A multiscale finite element model of a stress fracture

Alexander Wingård

2014

LUND
UNIVERSITY

Master's Thesis

Faculty of Engineering, LTH
Department of Biomedical Engineering
Supervisors: Hanna Isaksson and Lorenzo Grassi

Abstract

Stress fractures are problematic type of fractures as they are prone to delayed and nonunions. In order to achieve healing and restore the bones mechanical aspects, invasive treatments such as attaching plates, nails and screws are sometimes needed to stabilize the bone and facilitate healing. These surgical treatments often cause discomfort and pain to the patient. Therefore different options need to be considered, in order to reach better result. The purpose of this study is to improve understanding of why stress fractures do not heal during daily activity, through the use of a multiscale finite element model. The presented study is also the first to use finite element modelling and analyses of the stress and strain concentration in a patient with atypical fracture at the femur.

With the use of clinical CT- and μCT images, finite element models of the whole femur and the stress fracture were established. The contact force generated by different daily activities is applied at the conjunction of the hip and the femoral head. An inhomogeneous isotropic material model with poroelastic features is implemented, where the Young's modulus is based on a set of densitometric relations.

The displacements of the organ model at the location of the boarder of the micro model is registered and then applied to the micro model. A comparative study of the stresses, principal strains, octahedral shear strains and fluid velocities both pre- and post-surgery is done. These parameters are of significant matter as they describe the deformation of the tissue and may provide some insight into the tissue differentiation. The predicted stress and strain state in the granulation tissue of the micro model and post-surgery organ model is studied and compared with different tissue differentiation theories.

The results indicate that the stress and strain concentration within the bony material of the micro model correlated well with the pre-surgery organ model. Each studied load case, representing normal activity, predicted that certain areas of the crack are under the influence of high values of principal strain in tension, octahedral shear strains and fluid velocities. They are of such magnitude that the soft tissue undergo large deformation, which describes the stress fractures poor ability to heal. The predicted values of the principal strain, octahedral strain and fluid velocity between the studied activities were almost equally large, this suggest that there is no specific type of activity that is more strenuous on the crack.

Preface

This master's thesis has been carried out at the Department of Biomedical Engineering at Lund University in collaboration with the Department of Clinical and Experimental Medicine, Orthopaedics at Linköping, during the spring and summer of 2014.

I would like to give my deepest thanks and appreciation to my supervisors Hanna Isaksson and Lorenzo Grassi for their patient, support, invaluable guidance and introducing me to the interesting field of Biomechanics. I would also like to give a special thanks to Per Aspenberg and Jörg Schilcer, that provided the necessary clinical patient images to make this project possible and the Biomechanics groups that welcomed me into their group.

Alexander Wingård

Lund, October 2014

Contents

1 Introduction

A stress fracture is an injury that originate from small micro cracks in the bones that are not been able to heal. As a repetitive load is applied over a longer period, the crack can either grow in size or generate new cracks that eventually form a fracture. Although both men and women of all ages have been diagnosed with stress fractures, many cases of stress fractures are related to repetitive activity such as running, ballet dancing, track and field running and military service (Bennell et al., 1999; Warden et al., 2006; Blank, 1987). Stress fractures may also occur in elderly with a bone degenerative disease named osteoporosis (Schilcher and Aspenberg, 2009). This type of stress fractures is believed to originate from the treatment of osteoporosis with drugs called bisphosphonates, and is known as atypical fractures. In many cases, atypical fractures are not diagnosed until it is too late and a complete fracture has occurred. Therefore they are often treated as complete fractures (Aspenberg and Schilcher, 2014).

Healing of a stress fracture is often a slow process. If the fracture do not heal with conservative treatment (i.e. with rest), a surgical treatment is required. Most surgical treatments of stress fractures in the femur are treated using intramedullary nailing. This treatment may cause discomfort and pain to the patient and can therefore not be considered an optimal treatment. In order to find new treatments, one must fully understand why the stress fractures do not to heal. Earlier studies suggested that bone heal through tissue differentiation from soft tissues under the influence of adequate levels of strain (Perren, 1979).

A relatively new treatment in the field of stress fractures that have showed promising result consists of a surgical procedure where the stress fracture is removed by drilling a hole over the stress fracture, thus creating a larger trauma. The mentioned surgical procedure has the potential to minimize the pain and discomfort of the patient. By enlarging the crack, one may assume that the bone is weakened. However an MSc project performed by Fågelberg (2012) demonstrated that this weakening has negligible effects in terms of bone strain and stress in the mid-diaphysis of the tibia.

The study of Fågelberg (2012) compared (on a macro level) the mechanical milieu in the crack ragion, in order to understand why the proposed treatment have shown promising result. The study involved a stress frac-

ture located at the anterior cortex of the tibal mid-diaphysis and it was modelled as a geometrical perfect shaped crack. The study modelled the bone as poroelastic (Få gelberg, 2012).

However, based on literature (Schilcher and Aspenberg, 2009) we know that the micro geometry of the crack is not a perfect plate shape. Therefore, the next step is to implement a model which describes a real geometrical stress fracture. Therefore modelling on different tiers of resolution will be the main focus of the current thesis. Fågelberg et al. looked at a stress fracture in a young athletic patient in the tibia. In this project, the stress fracture is an atypical fracture located at the femoral shaft from an older lady. Performing a comparative study on different tiers of resolution may provide a deeper understanding of the structural and biological behaviour of stress fractures and treatment. Since a different bone is studied (i.e femur instead of tibia) it may tell if the drilling surgery can successfully be applied in other bones than the tibia. Overall three models will be compared: two representing an organ model of the femur pre- and post-surgery. The third model represents the stress fracture on micro level. The study includes stress and strain analysis, application of boundary conditions representing daily activities. Finally, the predicted strains are analysed according to a tissue differentiation theory, in order to understand whether stress fractures was able to heal.

1.1 Aim

- Create an accurate Finite Element multiscale model based on two different tiers of resolution of a stress fracture in the femur. A macro model representing the whole femur and a micro model covering the stress fracture will be compared.

- To analyse the stress and strain concentration in a stress fracture from patient with atypical fracture.

- To apply a tissue differentiation theory under normal daily activity loading, and reach a better understanding of stress fractures inability to heal. Finally, the potential of the surgical approach will be tested as a modelling exercise.

2 Background

2.1 Human bone

Bone together with muscles are one of the main components that keeps the body moving. Their most important functions are to absorb forces, protect vital internal organs and act as a source of minerals and production of blood cells for the rest of the body (Van C. Mow, 1997).

In 1892, Julius Wolff postulated that bone was either formed through modelling or remodelling dependent on the mechanical stimulation it was subjected to (R. Bruce Martin and Sharkey, 1998). By other means, the bone adapts and modifies its structure depending on the mechanical loads.

As any other materials, bone breaks when it is subjected to a force that exceeds its ultimate strength. Through remodelling, bone has the remarkable ability to heal and repair itself and return to its former strength without leaving any sign of trauma. Remodelling is a process that is ongoing throughout our whole life. Bone modelling is mostly seen at a younger age where the bones undergo huge size and shape transformations. The modelling and remodelling is regulated by cells originated from the stem cells (Mesenchymal stem cells, MSC). There are osteoclasts that removes (resorb) bone, osteoblast that form bone and osteocytes that are believed to orchestra the remodelling process (R. Bruce Martin and Sharkey, 1998).

In order to get a more understandable view of bone structure, the bone is divided into different hierarchical levels (figure 1), they are:

- **Macro structure**: cortical and cancellous bone.
- **Micro structure**: Haversian systems, osteons and single trabeculae.
- **Sub-microstructure**: lamellae and woven bone
- **Nano-structure and Sub-Nano-structure**: collagen fibres, whereas collagen molecules, non-collagenous proteins and mineral crystals are the building blocks of theses fibrils.

Cortical bone forms the diaphysis of long bones and the surrounding shell of the metaphysics (the border between the epiphyseal and the diaphysis region). The porosity of the cortical bone varies between 5-10%. Studying a internal structure of the cortical bone, small canals can be seen, they are

known as Haversian canals (osteons) and Volkmanns canals, figure 1. The Haversian canals contain capillaries and nerves and the Volkmann canal connect the Haversian canals to each other and to the surface of the bone (R. Bruce Martin and Sharkey, 1998).

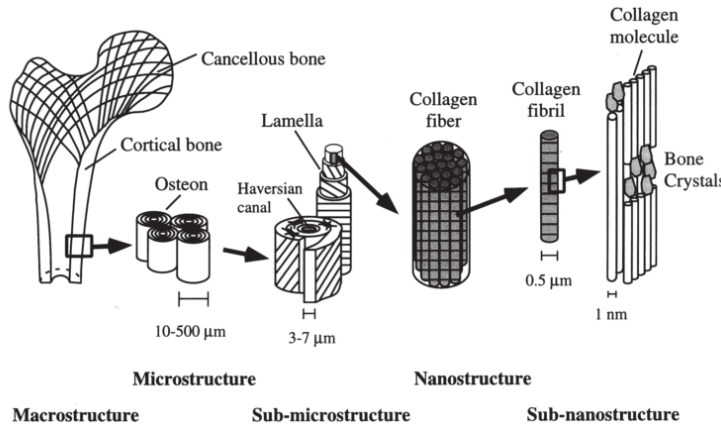

Figure 1: Hierarchical structural organization of bone (Rho et al., 1998).

Trabecular bone is also known as cancellous or spongy bone mainly because of its porous structure, with porosity ranging between 75-95%. Trabecular bone can be found in flat bones, distal or proximal ends of the long bones and in connective areas next to the hollow cavity known as the marrow. The marrow works as storage and producer of blood cells (R. Bruce Martin and Sharkey, 1998).

At a smaller scale of resolution (microscopic level) cortical and trabecular bone can be divided into two subgroups: Lamellar bone and woven bone. What separates these two groups is their structure. Lamellar bone grows at a slower rate, however it is a more organized bone where the collagen fibres are aligned parallel to each other. Woven bone grows in a more random orientation and at a faster rate. It is mostly seen during fracture healing (Van C. Mow, 1997). From a mechanical point of view, woven bone is weaker than lamellar bone (Stephen C. Cowin, 2007).

2.1.1 Density

The total volume of a bone can be divided into two parts: one hard bony matrix, and voids filled with fluid. These two parts have different ratio between mass and volume, i.e. density. Several definitions can be given for bone density. The most common ones used in literature are:

- **Bone mineral density** (BMD), the amount of mineral (hydroxyapatite) per volume unit in the bone.
- **Apparent density** (ρ_{app}), specified as the fraction of mass of the volume bone.
- **Ash density** (ρ_{ash}), the amount of mineralization of the bone. Ash density is calculated as the ratio between the mass of the burnt bone and the volume of the bone.
- **Radiological density** (ρ_{qct}), specified as the amount of bone necessary to provide the same attenuation to X-rays of calibration sample of known density. By other means, the bone sample shares the same attenuation to X-rays as a phantom with a known density.

The relations between these different definitions of density will be discussed later.

2.1.2 Poroelastic behaviour of bone

As bone has a porous structure with fluids inside the voids, modelling bone as a standard linear continuous model may not capture its actual behaviour. By other means, implementing a poroelastic model of the bone describes its structure more accurately. In 1941 Biot published an article regarding poroelastic theory (Biot, 1941). The general idea of his theory is that the material model is structured of two phases, one solid phase and one fluid phase. The solid phase covers the solid material and the fluid phase covers the fluid in the voids (pores) between the elements within the solid matrix. As the porous material is subjected to forces it generates strains and stresses within the structure, physically the generated strains and stresses can be divided into two parts: hydrostatic pressure, which originates when the water is filling the pores and the average stresses within the solid structure. The properties needed to describe a poroelastic material are porosity,

permeability, Young's modulus, shear modulus and Poissons ratio of the solid and the fluid phase. Although Biot's theory of poroelastic models describes soils, it has been widely used in other porous structures such as bone or other biomaterials. Although bone is a viscous material, the viscous effect has a low impact on the structural stiffness and the strain distribution of the bone (Cristofolini et al., 2010), when loaded in physiological strain rates.

2.1.3 Mechanical behaviour of bone

Muscle forces can load bones in tension, compression and shear. The bone needs to be able to withstand a large amount of forces without breaking. The bone need to be stiff and strong. On the other hand, if the bone is too stiff it will be more brittle (R. Bruce Martin and Sharkey, 1998). The solution to this is the bones two-phase structure, minerals and collagen. The minerals of the bone consists primarily of calcium and phosphate. These two minerals form a hydroxyapatite crystal which stands for 60% of the bones weight. The remaining 40% is a mix of 10% water and the remaining 30% is an organic matrix, primarily made of type I collagen. In terms of volume, 40% is minerals, 25% is water and 35% collagen (Nordin and Frankel, 2012). Collagen gives the bone its flexibility and tensile strength, and the minerals give the bone its stiffness.

Stiffness, ductility and strength are few parameters that describes the materials mechanical behaviour. The relation between them are often studied in a stress versus strain diagram. Stress-strain diagrams can be used to extract several material parameters: the elastic modulus of a material is the slope of the linear part of the stress-strain curve (figure 2) (Nordin and Frankel, 2012). Yielding is defined as the point where the material is starting to deform plastically. From the yielding point, yield stress and strain values can be identified. At the end of the stress-strain curve rupture occur: the area described by the whole stress-strain curve gives the energy that the material can absorb before fracture. Keaveny and Hayes (1977) performed a study in which they established the relation between stresses and strains for cortical and trabecular bone, the relation can be seen in figure 2.

In figure 2 it can be seen that the slope of cortical bone is steeper than cancellous bone, by other means cortical bone has a higher Young's modulus,

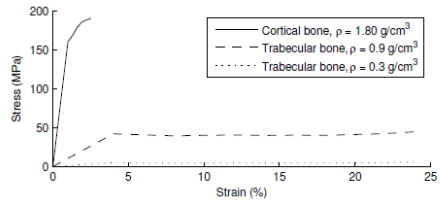

Figure 2: Stress strain curve Cortical and Trabecular bone.

though the strain cortical bone can absorbed is lower. The strain limit cancellous bone can exceed before breaking is roughly 10-50%, whereas cortical reaches its limit after only 1.5-2%. The high amount of energy cancellous bone can absorb is due to its porous structure (Nordin and Frankel, 2012).

Though cortical and trabecular bone are differently structured both mechanically and visually, they show some elastic similarities. Both cortical and trabecular bone show an anisotropic behaviour (different mechanical behaviour in different directions). The osteons in the compact bone show a transversely isotropic behaviour. Conversely lamellar bone shows a more anisotropic symmetry (Stephen C. Cowin, 2007). This leads to that compact bone is better adapted to resist stresses along its longitudinal axis, and it is more resistant to compressive loads than to tensile ones (Van C. Mow, 1997).

2.2 Stress Fracture

Stress fractures results from structural fatigue and cause localized pain and tenderness. Although the load is lower than the bone strength, when repetitive loads are applied under a longer period they can cause the crack to increase in size through fatigue failure. Factors of getting a stress fracture can either be extrinsic or intrinsic risk factors (Warden et al., 2006). Extrinsic factors are related to the type of activity such as training, the type of equipment that is used during an activity, and the environment. For example there has been numerous reports on runners, ballet dancers and military recruits that have suffered from stress fractures (Bennell et al., 1999). Intrinsic factors involve skeletal, muscle, joint and biomechanical factors. As an example, the loss of bone mass or reduced bone remodelling.

Micro-cracks appear in almost every bone in the human body, many of them as a result of cyclic loading. In most cases they heal by themselves through the remodelling process. In case there is not sufficient time for the bone to remodel, or a sudden increase of load in the meantime, the crack may grow in size, or even new cracks can form. This might lead to the formation of a macro crack known as a stress fracture (Van C. Mow, 1997).

Stress fractures are mostly located in the long bones, especially at the tibia. However, fractures located at the foot, spine, pelvis and femur have also been diagnosed. A factor why stress fractures are most commonly occurring in the long bones is the small cross-sectional area (Bennell et al., 1999). A bone with a large cross-section area is more resistant to fractures than a bone with a smaller, due to the internal forces being distributed over a larger surface area which lower the stresses in the bone. By other means a shorter bone with a larger cross-section area is more preferred in context of stress fracture resistance.

2.2.1 Atypical fracture

Stress fractures located at the femur are not as common as at the tibia. Most of these femoral stress fractures are either located at the femoral neck or at the femoral shaft. Many of them are either related to overuse, age or bone degenerative disease (Bennell et al., 1999).

Osteoporosis is a progressive bone disease that gradually decreases the mass and density of the bone. By giving the patient bisphosphonate the degenerative process of bone tissue removal is either slowed or stopped. As a side effect of such a treatment, the remodelling process is reduced (Schilcher et al., 2011). And since the bone-remodelling has slowed down, the repair of the bone micro cracks has stopped, or slowed down.

Bisphosphonate treatment increases the bone mineral density and matrix homogeneity. These factors facilitate the formation and propagation of cracks, as a high mineral content makes the bone brittle and cracks propagate easier through a homogeneous matrix (Schilcher et al., 2014). Stress fractures related to bisphosphonate treatment of osteoporosis has seen an increase over the last decade. This type of fracture is known as atypical fracture (Schilcher and Aspenberg, 2009; Schilcher et al., 2011).

2.2.2 Treatment

In general, stress fractures located at the femur are treated using internal fixation methods such as intramedullary nailing. Intramedullary nailing (IM) is a method where a rod is inserted in the medullary canal of the bone in order to fixate the fracture. Screws are used to get an increased stability and reduce the mobility of the fracture . Fixation of the femoral neck and head can either be done using external or internal applications, or in some cases replace the proximal part of the femur by an implant. Most of the patients that has been diagnosed with an atypical fractures is treated using IM nailing.

A method that has been under evaluation in previous master thesis projects, Fågelberg (2012) and Thesleff (2013) is a procedure where a hole is drilled at the site of the stress fracture. By drilling a hole through the anterior cortex the medullary cavity (thus removing the fracture), a larger trauma is created. The natural response of the body to the trauma is to initiate a healing process. The advantage of this method is that it is a relatively simple procedure. Therefore, the risk of getting any complications identified with insertion, attachment and removal of implants is reduced. This procedure has only been used at the tibia in young patients with good healing capacity.

2.3 Bone Healing

Trauma occur when the amount of energy that the bone can absorb is exceeded. The natural response of the body is to create a healing process, which can be divided into two types of healing dependent on the complexity of the fracture: primary- and secondary healing.

If the gap between the fracture ends is small, primary healing can occur. The primary healing works through the Haversian systems from the two fracture ends and creates a connective bridging, thus closing the gap. This process is relatively slow and requires high stability (Mckibbin, 1978).

The secondary healing involves the formation of a callus and can be divided into three partly overlapping phases: the inflammatory-, reparative- and the remodelling phase. Secondary healing can either be endochondral- or intramembranous ossification. The difference between them is that the endochondral ossification are bone differentiated from cartilage and in-

tramembranous ossification forms bone directly without any involvement of other tissues (R. Bruce Martin and Sharkey, 1998). Endochondral ossification is the most common one and produces the majority of the bones in the body.

Immediately after trauma, the broken blood vessels and periosteum creates a blood clot (hematoma) surrounding the fracture. The hematoma acts as first factor initiating the healing process. It supplies the process with the needed cells but also stops the blood flow and creates some initial low stability. This is known as the inflammatory phase and lasts for 3-7 days.

The reparative phase starts at the periosteum and at the marrow, creating a callus around the fractured ends. Even the smallest trauma activates the periosteum and the marrow to produce a larger amount of osteoblast. At a high rate an arch of hard callus is produced by the osteoblasts, mainly consisting of woven bone, which connects the two fractured ends together. Inside the gap, a softer callus can be found, mainly made of connective tissue (R. Bruce Martin and Sharkey, 1998; Claes and Heigele, 1999). As the endochondral ossification progresses more cartilage differentiates to bone, making the callus bridge. The reparative phase lasts for about one month. The newly formed bone has almost the same rigidity as before fracture, even though the callus material is not as strong as cortical bone. This is mainly due to the larger cross-sectional area (R. Bruce Martin and Sharkey, 1998).

After the reparative phase, the broken bone has almost the same strength as the bone before the fracture. However its size and mass are substantially higher. In the remodelling phase, the bone restores itself to the original shape and structure.

2.4 Tissue differentiation

Through endochondral ossification, soft tissues are able to differentiate to harder tissues such as bone. This process is highly dependent on the mechanical stimulation. There are many different theories trying to explain how this process occur. Three of these theories will be described in the following.

2.4.1 Pauwels

One of the first theories on tissue differentiation was hypothesized by the German scientist Friedrich Pauwels in 1960. According to Pauwels it was not possible for the stem cells to directly form bone from the granulation tissue, instead there were a couple of sub-steps that had to be taken before new bone could formed. High levels of strain in the soft tissues induce their differentiation into fibrous connective tissue, whereas hydrostatic pressure stimulations induce differentiation into cartilaginous tissue. Through the endochondral ossification woven bone could be formed, which later ended up in lamellar bone through remodelling. The differentiation theory can visually be seen in figure 3.

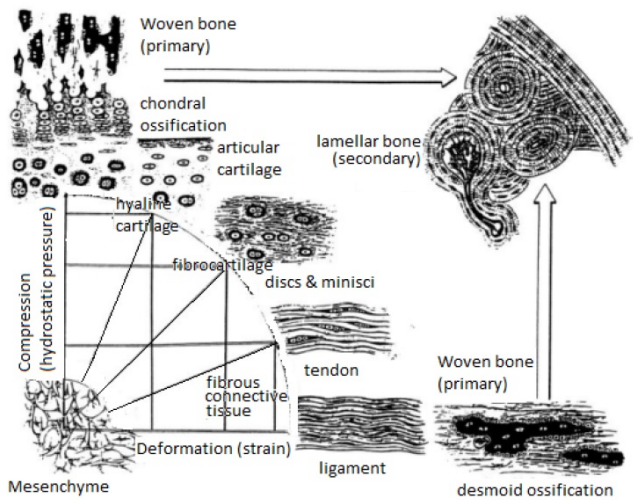

Figure 3: Pauwels tissue differentiation theory (Pauwels, 1960).

2.4.2 Perren and Cordey

In 1980 Perren and Cordey tried to quantify the strain thresholds at which tissues could differentiate to other tissue types (Perren, 1979). According to Perren and Cordey the type of tissue formed was related to the inter-fragmentary strain of the tissues. Their theory said that if the tissue was exposed to tensile strains that exceeded the rupture limit of the tissue, it

could not be formed. They estimated the strain thresholds for different tissues accordingly to table 1.

Tissue	Rupture limit
Bone:	0-2%
Cartilage:	2-10%
Granulation tissue:	10-100%

Table 1: Rupture limit for different tissue types according to the theory Perren and Cordey (Perren, 1979).

2.4.3 Prendergast and Huiskes

A later theory in the field of tissue differentiation was developed by Prendergast and Huiskes in 1997. Different to earlier studies they modelled the bone as a biphasic material, by other means bone was modelled with poroelastic features (Huiskes et al., 1997; Prendergast et al., 1997). Their studies was done using an experimental based Finite element model. Based on the model, they showed that the applied force had a huge impact on the deviatoric strains (i.e. tissue deformation), fluid pressure and interstitial fluid velocity during the tissue differentiation (Prendergast et al., 1997). They hypothesised that the two most significant factors of the MSC differentiation is the fluid velocity in the pores and the deviatoric strain within the solid matrix. The deviatoric strain is equal to the octahedral shear strain γ, given by:

$$\gamma = \frac{2}{3}\sqrt{(\varepsilon_1 - \varepsilon_2)^2 + (\varepsilon_2 - \varepsilon_3)^2 + (\varepsilon_3 - \varepsilon_1)^2} \tag{1}$$

$\varepsilon_{i=1,2,3}$ describes the principal strains along each axis.

In order to describe the tissue differentiation, Prendergast and Huiskes introduced an index. The index (equation 2) is based on the octahedral shear strain (equation 1) and the fluid velocity. Whereas the threshold values describes the differentiated tissue and the values are based on measurements and literature data, the values for each formed tissue can be seen

in table 2 (Huiskes et al., 1997).

$$index = \frac{\gamma}{0.0375} + \frac{v_f}{0.003} \tag{2}$$

The fluid velocity v_f is in mm/s.

Tissue	*index*
Resorption:	$i \leq 0.010$
Mature bone:	$i > 0.01$
Immature bone:	$i > 0.267$
Cartilage:	$i > 1$
Fibrous tissue:	$i > 3$

Table 2: Threshold vales for the tissue differentiation according to the theory of Prendergast and Huiskes (Huiskes et al., 1997).

2.5 Computed tomography

In the biomedical field computed tomography (CT) images can be used to diagnose patient with different diseases, or to detect internal flaws in materials. Within this project, CT is mainly used to obtain three dimensional geometries of the investigated bone segments (Snyder and Schneider, 1991; Morgan et al., 2009; Taddei et al., 2004).

Computed tomography is a computer based scanning technology that emits X-rays on to an object to generate a set of tomographic[1] grey scale images. The slices can be piled to create three dimensional datasets, i.e. by stacking each slice on top of the previous slice.

Each section is produced using an X-ray transmitter that rotates around the object in a helical swept motion. The grey level of each pixel is a function of the material attenuation coefficient to X-rays (AC). The AC is a measurement on how efficiently light, sound and particles can pass through a material. The unit of measurement of radio density is the Hounsfield units (HU). HU is a linear relationship with the attenuation coefficient (Snyder and Schneider, 1991). The Hounsfield unit are obtained from the AC by

[1]Imaging a three dimensional object in sections

assigning a value of -1000 to air, and 0 to water (Taddei et al., 2004). The linear relation between HU and AC can thus be described as followed:

$$HU = 1000 * \frac{\mu_X - \mu_{water}}{\mu_{water}} \tag{3}$$

μ_{water} is the attenuation coefficient for water.

2.5.1 Micro computed tomography

Micro computed tomography was first developed at the Ford Motor Company, mainly to detect small defects in ceramic materials. However it quickly found usage in the medical field as well (Waarsing et al., 2004).

There are two types of micro CT-scanners: one uses the same principals as a medical CT-scanner (X-ray transmitter/detector rotating around the specimen), and the other where the object is rotating around the scanner. The advantage of using a micro CT scanner is that it can create slices at a higher resolution of the detector, at a higher dose of radiation (Morgan et al., 2009).

2.6 Finite element & Multiscale modelling

2.6.1 Finite element modelling in the biomedical field

The use of finite element modelling (FEM) on different length-scales has over the years been a useful tool in the biomedical field, due to lower costs and faster solutions compared to experimental studies. FEM has been used to estimate fracture risk, stress/strain distribution, and simulations of bone healing etc (Schileo et al., 2007; Isaksson et al., 2006; Claes and Heigele, 1999). The results of FE simulation has showed to be accurate under the condition that the boundary condition and material properties are described properly (Morgan et al., 2003; Taddei et al., 2007; Schileo et al., 2007, 2008).

Many studies focused only on one tier of resolution, despite bone structure appears to be heterogeneous at different length scales. Studying bone behaviour at different resolutions may give a better understanding on how loads applied on macro level may affect the structure at the micro level.

2.6.2 Multiscale modelling

In order to fully understand the structural changes that occur in an object when it is subjected to loads, the simulation can be solved on different length-scales.

When an object is subjected to loads, the scale of resolution may not be enough to understand what is happening on the structural level. By lowering the scale of resolution or solving the simulation on different tiers of resolution, a deeper knowledge may be reached. This is an engineering technique known as Multiscale modelling, where different models are used on different tiers of resolution, i.e. different length scales, interact with each other to achieve the final result.

Multiscale models can be divided into different types, according to how the interaction is implemented between the different blocks: Type 1, Type 2 and Type 3 according to figure 4 (Walpole et al., 2013).

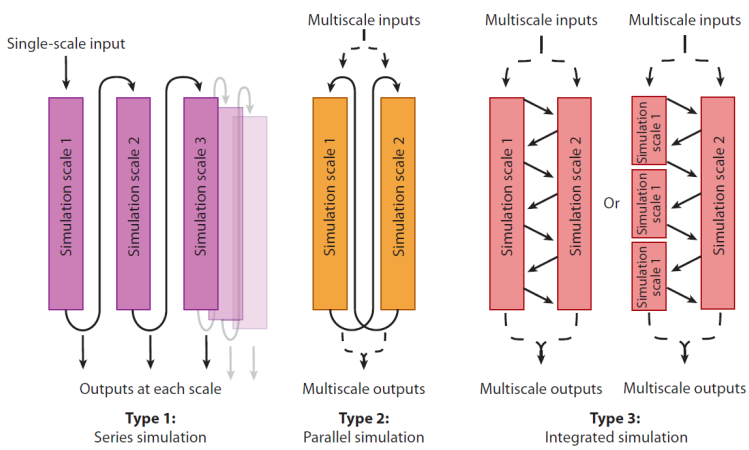

Figure 4: Different types of multiscale models according to (Walpole et al., 2013).

- Type 1: An iterative approach in which the result from each simulation is transferred to the next simulation scale, and a later tier of resolution has no ability to affect the result of an earlier tier.
- Type 2: Each simulation are independently solved to generate result for the other simulations. As figure 4 shows, information from each

simulation can be passed between the simulations and affect the final output, though this can only be performed after the simulation is solved.

- Type 3: Each simulation is run in parallel with each other, and the information are allowed to constantly jump between the simulations and progressively affecting the results.

In this thesis work a type 2 will be used a first approach.

3 Materials

The present study is conducted on the subject of a woman diagnosed with an atypical stress fracture. The woman was 83 years old at the time of the stress fracture, and was treated with cortisone for her asthma. A CT scan of the hip, left and right femur was taken at Linköping University Hospital. The stress fracture was located at the lateral side of the left femur mid-diaphysis. The surgeon took a biopsy surrounding the crack by drilling a hole over the crack. Thereafter, the woman was treated by inserting an intramedullary nail. Two cross-section images can be seen in figure 5; the image to the right shows the posterior view of the femur and hip, whilst the image to the left shows the superior view of the femur.

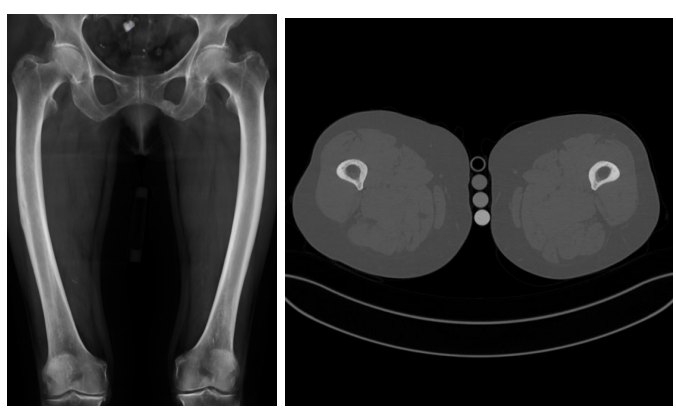

Figure 5: CT images on macro level.

After surgery, the extracted bone biopsy containing the crack was im-

aged using a micro computed tomography scanner (μCT) (Desktop Skyscan, anteselaan, Belgium). This generated a set of images showing the structure of the stress fracture and the surrounding bone at a voxel size of 15 micrometres. Two cross-section images can be seen in figure 6, the image to the right shows a section in the internal part of cortical bone, whereas the image to the left shows the crack on the external surface of the cortical bone specimen. One can see that the porosity is increasing as we go into the bone.

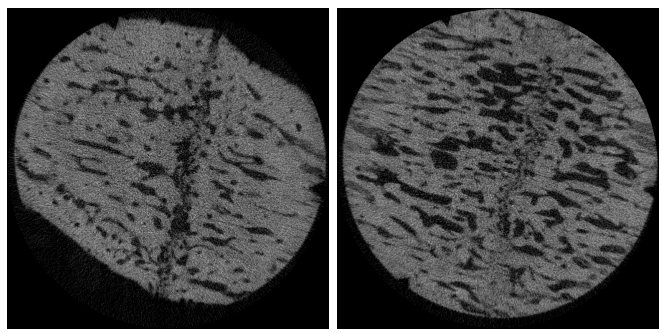

Figure 6: micro CT images with 15μm voxel size.

4 Methods

A multiscale model of the femur and the stress fracture was developed using FEM. The description of the methods will be structured into sections: Geometry, Mesh, Material modelling and Boundary conditions. The connection between the different models at different length scales can be seen in figure 7.

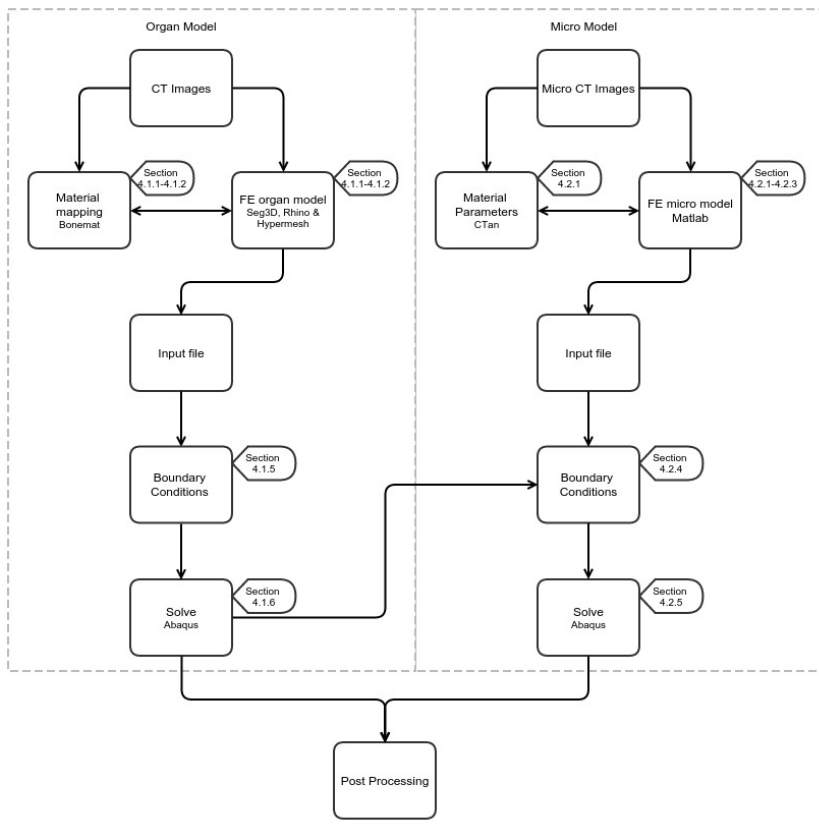

Figure 7: Flow char and strategy on solving the project.

4.1 Finite Element Modelling in current project

The multiscale model is divided into two parts, one described as the organ model (modelling of the femur from CT scan data), and the second as micro model (modelling of the stress fracture adn surrounding bone from micro-CT images of the extracted bone biopsy). Although the micro model is dependent on the result from the organ model, the two FE models can be generated simultaneously. At the organ level a load is applied to the femoral head, and the resulting displacements at the boundary for the biopsy retrieved. The calculated displacements are thereafter transferred to the micro model according to figure 7.

During the treatment of the patient a nail was inserted into the medullary canal of the femur, to stabilize the bone. The nail will not be modelled, which will affect the stress and strain state of the post-surgery organ model. Instead, a theoretical exercise will be conducted where the patient also is investigated post drilling but without the nail instead. This is to be able to theoretically compare the results with those by Fågelberg et al. (2012).

4.2 Organ model

The FE model for the femur was conducted using a procedure proposed by Schileo et al. (2007), which have been validated previously and shown accurate in terms of strain prediction. The following procedure was used:

1. Detect the bone geometry through CT segmentation.
2. Reverse engineering (NURBS extraction) and meshing of extracted surfaces.
3. Definition of the material properties using densitometric calibration of the CT dataset. And a numerical integration algorithm to assign the elastic modulus to each element.

The organ model comprises two models, one pre-surgery and one after removing the biopsy through drilling surgery but without inserting the nail. The geometry is defined in the same way, but the material properties in the cracked region are modelled with different material properties, as will be explained in section 4.2.3.

4.2.1 Geometry

Geometry extraction
The organ model consists of different parts and was produced by different segmentation techniques, later they were matched and put together to a larger three dimensional model. Segmentation is a technique where the boundaries between tissues are defined. In most cases automatic algorithms together with a manual correction (if needed) are used to segment structures (Viceconti and Taddei, 2003). Both the femur and the marrow were segmented from the CT images, however the extraction of the two contours was done using different methods.

Segmentation of the external contour of the femur was performed using a threshold function. The threshold value was changed until there was a distinctive border between the bone and soft tissue. As a complete shell was not obtained, the surface had be manually closed using a brush tool in some anatomical locations. After an external surface was obtained, the internal holes could be automatically filled in the software using a dedicated tool. The whole operation was performed in Seg3D (version 2.1.5, Scientific Computing and Imaging (SCI), Utah, USA). The binary matrix of the segmentation was exported and a StereoLithography (STL) geometry of the femur was created. A STL geometry consists of a three dimensional description of a surface using triangular elements.

The segmentation of the marrow was performed using an edge-driven snake, which works as follows: A threshold was chosen in the same way as for the external boarders, to define a region of interest where the snake is allowed to grow. Then, some spheres (small snakes) are manually placed over the region of interest, and expanded according to a mathematical equation that guides the expansion as a function of the grey level gradients in the images (Kass et al., 1988). The snakes growing was manually interrupted when they reached the beginning of the epiphyseal. Segmentation of the marrow was done in ITK Snap (Yushkevich et al., 2006).

The relative position of the extracted bone sample (imaged with micro-CT) with respect to the whole femur (imaged with the clinical CT) was determined via a manual registration of the two geometries (LhpBuilder, version 1.5, Biomed Town), aimed at aligning the two crack regions. This operation was performed with the supervision and final approval of experiences medical personnel.

4.2.2 Mesh

The generated NURBS surfaces for the femur, marrow and the cylinder (representing the extracted cracked bone sample) were imported into HyperMesh. With the help of built-in tools a connection between the three bodies was created. When a connection had been established, the three parts were meshed separately using an automatic two dimensional triangular surface element function. To minimize the computational cost of the FE simulation, different element sizes were chosen depending on the location. Near the crack, a fine structured mesh was built, which means that the elements have a smaller size and therefore there is a greater number of elements at that location. Element size increased, and thus the mesh got progressively coarser when walking away from the crack region. This was mainly done in order to reduce the computational cost.

The mesh was created using the two dimensional surface mesh for the three bodies as a reference. As before a coarser element mesh was chosen closer to the epiphysis, to save computational cost. The quality of the mesh was checked and distorted or bad quality elements were refined. The meshed femur can be seen in figure 8. The three dimensional mesh was generated using second order ten node tetrahedral elements (C3D10MPH in Abaqus). The M stands for modified, P pore pressure and H that the elements are a hybrid with linear pressure. The described ten node tetrahedral pore pressure element is a hybrid that have one additional variable relating the effective pressure stress (Abaqus, 2012). The same element was used in earlier master thesis project Fågelberg et al. (2012).
The total amount of element and nodes used in the organ model is reported in table 3.

Total elements:	417795
Total nodes:	631522
Number of elements at the hole:	8373
Number of nodes at the border:	2640

Table 3: Number of elements and nodes in the organ model.

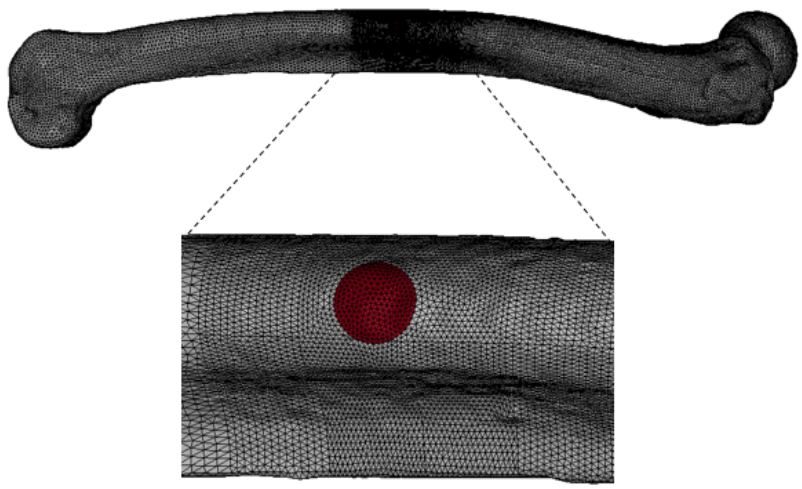

Figure 8: Element mesh of the femur and the placement of fracture.

4.2.3 Material modelling

In order to model bones porous structure, proper material parameters needs to be assigned to the elements. The material parameters needed in the model can be seen in table 4. The material parameters that describes the porous structure of bone are based on experimental values and the parameters regarding Young's modulus is based on densitometric calculations. The second step of the FE geometry generation was to determine the density-elasticity relation, which in most cases is implemented as a power-law function. As mentioned in section 2.1.3, bones is anisotropic. Modelling bone anisotropy would be desirable, it is not possible to accurately extract the main direction of anisotropy from clinical CT-images. Each element will thus be assumed to be isotropic with a Young's modulus assigned as a function of the bone density at that specific location.
Density-elasticity relationship
A powerful tool to estimate the bone density is the use of a bone phantom. A phantom is a set of tubes containing a bone equivalent material with known densities. As the phantoms is scanned, the Hounsfield unit (HU)

Parameter	Symbol	Description
Young's modulus	E	Defines the stiffness of the material
Possion's ratio	ν	The negative ratio of transverse to axial strain
Permeability	k	A materials ability to transmit fluids through the pores
Solid bulk modulus	K_s	Defines the solid's resistance to uniform compression
Fluid bulk modulus	K_f	Defines the fluid's resistance to uniform compression

Table 4: Definition of material parameters.

for each tube can be determined using an imaging software, in this case Fiji (Schindelin et al., 2012). Then, assuming a linear regression between the radiological density and the average HU, the calibration constants for the model can be derived. This procedure allows to calculate the bone density from the voxel values of the CT scan in each point. As an appropriate bone phantom was not imaged together with the patient in our case, a European Spine Phantom (ESP) was imaged separately on an equivalent CT-scanner, using similar scanning parameters. ESP is a standardized phantoms, where the bone equivalent material is Hydroxyapatite. ESP is intended to be used as a quality control of other phantoms but also to cross-calibrate CT devices around Europe (Kalender et al., 1995). The resulting calibration equation is:

$$\rho_{qct} = 0.000792174 * HU - 0.004132330 \tag{4}$$

In a study performed by Schileo et al. (2007), it was found that the most accurate way to describe the relation between the radiological density (ρ_{qct}) and the ash density (ρ_{ash}) is with a linear relationship, known as a calibration correction. The final expression looks as follows:

$$\rho_{qct} = -0.09 + 1.14 * \rho_{ash} \tag{5}$$

In the same study they also found a constant ratio between ash density and apparent density given by ρ_{ash}/ρ_{app}=0.6. Together with equation 4 and 5 the apparent density can be expressed as a function of the HU as:

$$\rho_{app} = 0.1255375 + 0.000694889 * HU \tag{6}$$

Elastic-density power-law relationship
There are numerous studies on how to derive the Young's modulus. Among this plethora of relations between bone density and Young's modulus. Morgan's power-law was chosen (Morgan et al., 2003). This power law has shown to provide high accuracy when implemented in FE simulations validated with experiments. Equation 7 displays Morgan's modulus-density relationship:

$$E = 6850\rho_{app}^{1.49} \tag{7}$$

The unit of Young's modulus is in MPa and ρ_{app} equals g/cm^3.

Material mapping
Material mapping is used to assign material properties to the model. To do so, two methods can be used: the first method calculates the average HU value over the element volume and then converts it to apparent density and Young's modulus. The second one calculates Young's modulus for each voxel and then calculates an average Young's modulus value over the element volume (Taddei et al., 2007). Although both methods work well, the second method provided slightly more accurate result when compared with experimentally measured strains and stresses (Taddei et al., 2007).

To perform the mapping of the mesh, CT-scan images and the calibration constants in equation 4, 5 and 7 can be given as an input to a software called Bonemat (Taddei et al., 2007). Based on the HU-value of the CT-image and the described equations, Bonemat calculates and assigns the elastic modulus for each element, no threshold value is needed. In table 5 the range of material parameters used in the organ model can be seen. In the model representing the post-surgery condition the elements located at the excised bone region were assigned material parameters corresponding to soft tissue (granulation tissue), whereas all the other elements kept the original material mapping.

4.2.4 Reference system

An anatomical reference system has to be determined over the femur in order to apply meaningful boundary conditions. The created reference system was chosen according to Bergmann et al. (1993). Three landmarks were used to apply the reference system to the model. These were placed at

Material properties	Bone tissue	Soft tissue
Young's modulus [MPa]:	366 – 18649	1
Poisson's ratio	0.3	0.167
Permeability (m^4/Ns)	$1.0{\cdot}10^{-17}$	$1.0{\cdot}10^{-14}$
Solid bulk modulus (MPa)	17660	2300
Fluid bulk modulus (MPa)	2200	2200

Table 5: Material properties assigned to the organ model, adopted from (Thesleff, 2013).

the following locations: The mid-point and the centre of the reference system was placed at the intercondylar fossa (IF). The second landmark was placed at the trochanteric fossa (TF). The third was placed at the centre of the femur head (FH) (Cristofolini et al., 2009). The z-axis is directed towards the TF respectively the x-axis towards the FH. The reference system defined is shown in Figure 9.

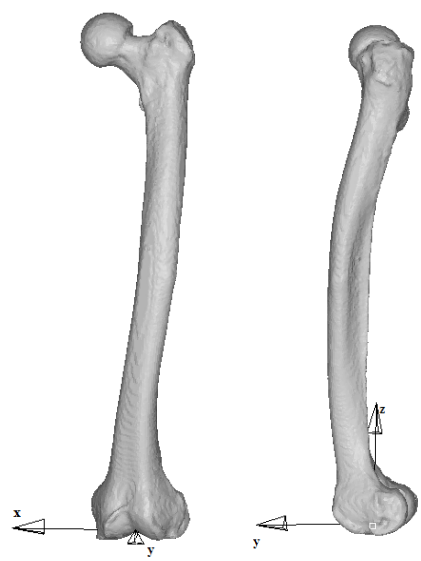

Figure 9: Anterior and lateral view of the femur.

4.2.5 Boundary conditions

During daily activities bones are loaded by body weight, muscles, contact forces, joints and so on. A desirable approach would be to implement all these loads. However, identification of muscle and contact forces is not possible in vivo for each specific subject. Therefore, the implemented boundary conditions of the organ model will only focus on the loads applied to the femoral head, as those have been estimated by previous studies (Bergmann et al., 2001).

Loads
Bergmann et al. (2001) performed an extensive study on the contact forces in the hip joint. They recorded the contact forces between the femoral head and the pelvis by replacing the femur head with a force sensitive implant. The contact forces were registered during different daily activities (such as walking, upstairs climbing, etc.) and kinematic data from gait analysis were recorded at the same time. The forces Bergmann et al. (2001) registered in their study were used to simulate the loading conditions of the femur.

In order to get an understanding of how the different daily activities affect the stress\strain pattern in a bone, different loading conditions were applied to the organ model. The loads change in magnitude and direction, due to the fact that the femoral head is moving around in its socket. In table 6 the different activities are represented, included in the table is the peak hip contact force and the angle of inclination of the force vector. The two registered angles were named Az and Ay (Bergmann et al., 2001). Az represents the angle in the transverse plane (the xy-plane). Ay is angle in the frontal plane (the xz-plane), according to the reference system in figure 9.

The boundary conditions for climbing stairs were chosen as they generate a larger bending moment on the femur (Bergmann et al., 2001). All angles are specified in degrees. The unit of load is in Newton, though it is reported as a percentage of the body weight. Each activity during one gait cycle generated force components in x-, y- and z-direction accordingly to figure 10, where the maximum register force (peak force) was registered at the first peak. The thick black line represent the resultant force vector

Activity	%BW	Ay	Az
Normal Walking	238	13	31
Fast Walking	250	12	30
Up Stairs	251	14	46
Down Stairs	260	12	35

Table 6: Peak force and the force vectors inclination angle during different activities.

and the thinner grey\black lines represent the force components. In figure 10 the force component in the z-direction is almost equal to the peak force, therefore they are assumed to be equal or slightly lower than the peak force. Using the tabulated values in table 6, the different force components were calculated and are presented in table 7. The loads are expressed in percentage of the body weight, which can be converted to Newton for each patient.

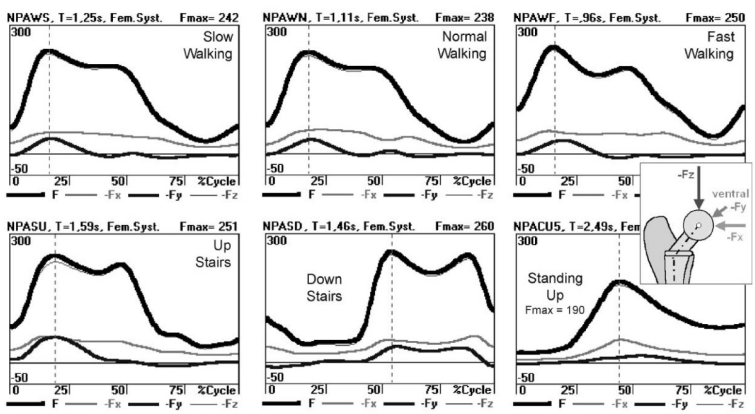

Figure 10: Generated forces during a gait cycle for each activity, adopted from (Bergmann et al., 2001).

As it is very difficult to estimate where contact between the pelvis and the femur head originate, a set of nodes were manually placed at the location where the contact was believed to originate from. The set of nodes where

Activity	$\%BW_X$	$\%BW_Y$	$\%BW_Z$
Normal Walking	54	33	235
Fast Walking	53	31	250
Up Stairs	60	62	240
Down Stairs	54	38	255

Table 7: Body weight percentage in in x-, y- and z-direction (Bergmann et al., 2001).

place slightly above where the ligamentum teres attaches to the head. Each node was assigned an average load in x-, y- and z-direction accordingly to table 7.

Locked nodes
To prevent any rigid movement of the organ model, the nodes at the distal extremity of the femur were locked in x-, y- and z-direction. The distal extremity comprises nodes from the contact point of the condyles and the tibia and up to the beginning of the diaphysis.

4.2.6 Abaqus implementation

In order to run simulation in Abaqus (version 6.12-4, Dassault Systems, France) an input file was created. The organ model used second order ten node tetrahedral elements. The ten node tetrahedral element type is chosen because first order tetrahedral elements have slow rate of convergence. The exported file from HyperMesh include all data for the elements, nodes and material properties, they were then structured into text files which were included in the input file for the FE simulations. Simulations were performed in Abaqus (v6.12, Simulia, Inc.).

4.3 Micro model

4.3.1 Geometry

The given phantoms for the micro CT images had a known density of 0.25 and 0.75 g/cm^3, respectively. When imaged, those two densities corre-

sponded to an attenuation constant of 0.01764 and 0.04264, respectively. The calibration was performed using the software CTan (version 1.9.3.2, Bruker, Kontich, Belgium). Within the software the known densities of the phantoms were matched with a grey-scale value of the μCT-images. Where the finally grey-scale threshold value was calculated based on fully mineralized bone (which was set to be equal to 0.642g/cm^3 (Bosemark et al., 2013)). The calculation was done by performing an interpolation between the densities and grey values of the phantom and the density of the mineralized bone. The threshold was calculated to 63.7.

Generating a micro model geometry can be done using different techniques. In this case the geometry was created using a Matlab code adapted from the work of an earlier master thesis project (Lugo, 2013). The geometry is created by first importing the micro-CT images and piling them in Matlab, the pile is then downsized. Secondly, each pixel in the image was read and was assigned as bone tissue or empty space depending on a grey-scale threshold value.

When implemented, Matlab generate a binary matrix which describes the geometry of the micro model, see figure 11. The empty space was later filled in order to represent the soft tissue within the micro model.

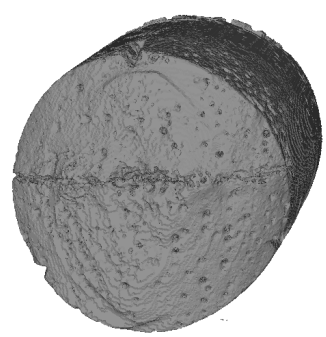

Figure 11: The geometry of the micro model. The crack can be seen horizontally.

4.3.2 Mesh

The binarized volume obtained as an output from the segmentation process was then converted into a FE model using Iso2mesh (Fang and Boas, 2009). Function vol2mesh was used in order to transform the binary matrix into

nodes and tetrahedral elements. For each element a grey-scale value was calculated.

The threshold value mentioned in section 4.3.1 was then used to divide elements in to two components, bone tissue and soft tissue. Elements with a grey-scale value below the threshold will be assigned as soft tissue (granulation tissue) and the rest will remain bone tissue.

As input parameters the user can define the maximum element volume and the surface density. These two parameters will affect the total amount of elements and nodes used in the model and therefore will affect the computational cost. It is recommended to use as evened sized elements as possible, as the result will be mesh dependent.

The total amount of elements and nodes used in the μCT model can be seen in table 8 and the final mesh can be seen in figure 12.

Total number of elements:	2279712
Total number of nodes:	362520
Number of elements, soft tissue:	608131
Number of elements representing the crack:	16687

Table 8: Number of elements and nodes in the μCT model.

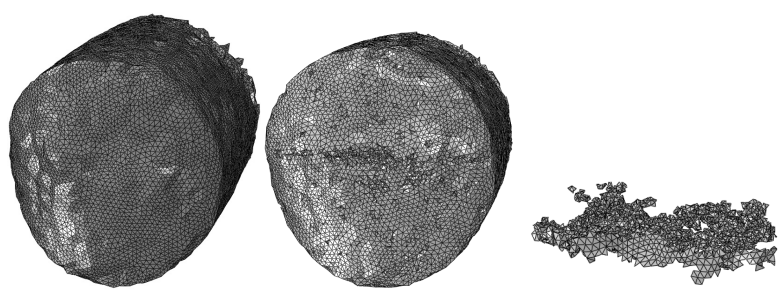

(a) (b) (c)

Figure 12: The mesh of the micro model geometry. (a) mesh of the whole micro model, (b) mesh of the bony material and (c) mesh of the crack.

4.3.3 Material modelling

In section 4.3.1 a calibration was performed to determine the threshold. At the same time the two calibration constants was given assuming a linear regression between the bone mineral density and the AC according to equation 8.

$$AC = 0.00514 + 0.05514 * BMD \tag{8}$$

Morgan's density-elasticity was again chosen for the micro model, the power-law is described as follows:

$$E = 6850 BMD^{1.49} \tag{9}$$

Each element has a calculated elastic modulus value, however assignment of the parameters for each element was done using a subroutine in Abaqus. As mentioned in section 4.3.2 the mesh was divided into two components, representing bone tissue and soft tissue (granulation tissue). The assigned material parameters for bone- and soft tissue can be seen in table 9. The micro model was modelled as poroelastic.

Material properties	Bone tissue	Soft tissue
Young's modulus bone [MPa]:	3485 – 13215	1
Poisson's ratio bone	0.3	0.167
Permeability (m^4/Ns)	$1.0{\cdot}10^{-17}$	$1.0{\cdot}10^{-14}$
Solid bulk modulus (MPa)	17660	2300
Fluid bulk modulus (MPa)	2200	2200

Table 9: Material properties assigned to the micro model.

4.3.4 Boundary conditions

To apply the registered displacements from the organ model to the micro model a Matlab code was used. In order to assign each surface node of the micro model with a displacement, the nodal coordinates of the micro model had to be reworked. To do so a transformation matrix (used to move a point in space, both in rotation and translation) was implemented. Using

a set of different transformation matrices the coordinates were changed so that the location, alignment and rotation matched the cylinder in the organ model. The transformation matrices were obtained as follows:

(i) The geometry of the micro model was pre-aligned manually using the organ model and a cylinder representing the excised bone as reference.

(ii) The front surfaces of the organ model and the micro model was aligned. To do so two different models were used: one describing the micro model and one describing the excised region from the organ model. These two where aligned using an automated algorithm that align points in the two models.

The displacement registered at the border between the organ model, and the excised bone was transferred to the micro model with the use of a Matlab code. The code assigns a boundary condition (displacements in x-, y- and z-direction) to all nodes in the micro model that lie within a tolerance, by other means the code finds the two closest nodes of the two models. The tolerance describes an acceptable nodal distance between the two models. The choice of tolerance is related to the element size, in this case a value of 0.7 comprises most of the nodes in the micro model.

4.3.5 Abaqus implementation

The Matlab code has a section where an Abaqus input-file automatically is generated. The file is used to run simulations in Abaqus. The file is structured in different sections: importing necessary data such as node and element definition, assigning material properties to the model, boundary conditions and output requests. The μCT model used first order tetrahedral elements (C3D4P in Abaqus). Although first order tetrahedral elements have slow rate of convergence, the element type was chosen because earlier master thesis project used the same element type to describe a bone biopsy sample on micro level (Lugo, 2013). The units of the micro model is defined in MPa (stress), N (force) and mm (length).

5 Results

5.1 Multiscale model

The applied load causes a variation in displacements within the structure of the organ model. The maximum and minimum registered displacement (in x-, y- and z-direction) for the nodes located at the external surface of the micro model are presented in table 10. The directions of the registered displacement are based on the coordinate system in section 4.2.4.

Activity	x-direction (mm)	y-direction (mm)	z-direction (mm)
Normal Walking	3.36±0.32	-2.44±0.25	-1.12±0.57
Fast Walking	3.34±0.32	-2.35±0.24	-1.20±0.62
Down Stairs	3.42±0.33	-2.79±0.29	-1.12±0.61
Up Stairs	3.74±0.36	-4.20±0.43	-1.12±0.76

Table 10: Registered minimum and maximum displacements at the region of the excised biopsy of the organ model.

As can be seen in table 10, the highest registered displacements occurred during climbing up stairs followed by walking down stairs. Climbing up stairs showed a significant larger displacement in the x- and y-direction, and fast walking showed a larger displacement variation in the z-direction. This is most likely because of the larger applied load in these directions. No other major displacement differences were registered between the different activities.

Based on these result, the von Mises stress (MPa) are presented, together with principal strains and fluid velocity (mm/s) for fast walking and climbing up stairs. The von Mises stress, principal strain and fluid velocity distribution can be seen in figure 13 and 14, respectively. The image to the left shows the organ model pre-surgery and to the right the frontal view of the micro model.

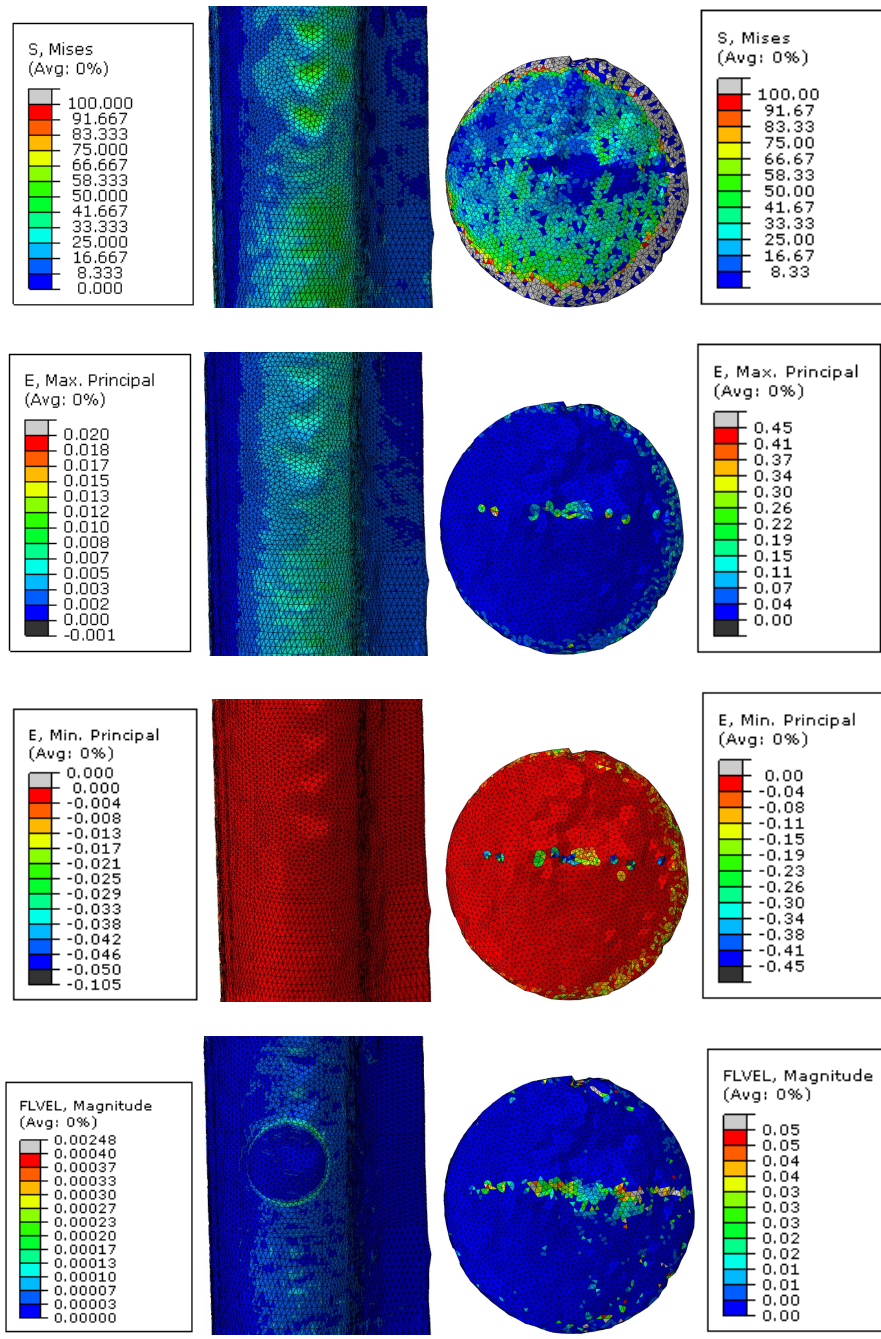

Figure 13: From top to bottom: The von Mises stresses, major principal strain and minor principal strain and fluid velocity during fast walking. To the left the organ model and to the right the micro model.

.

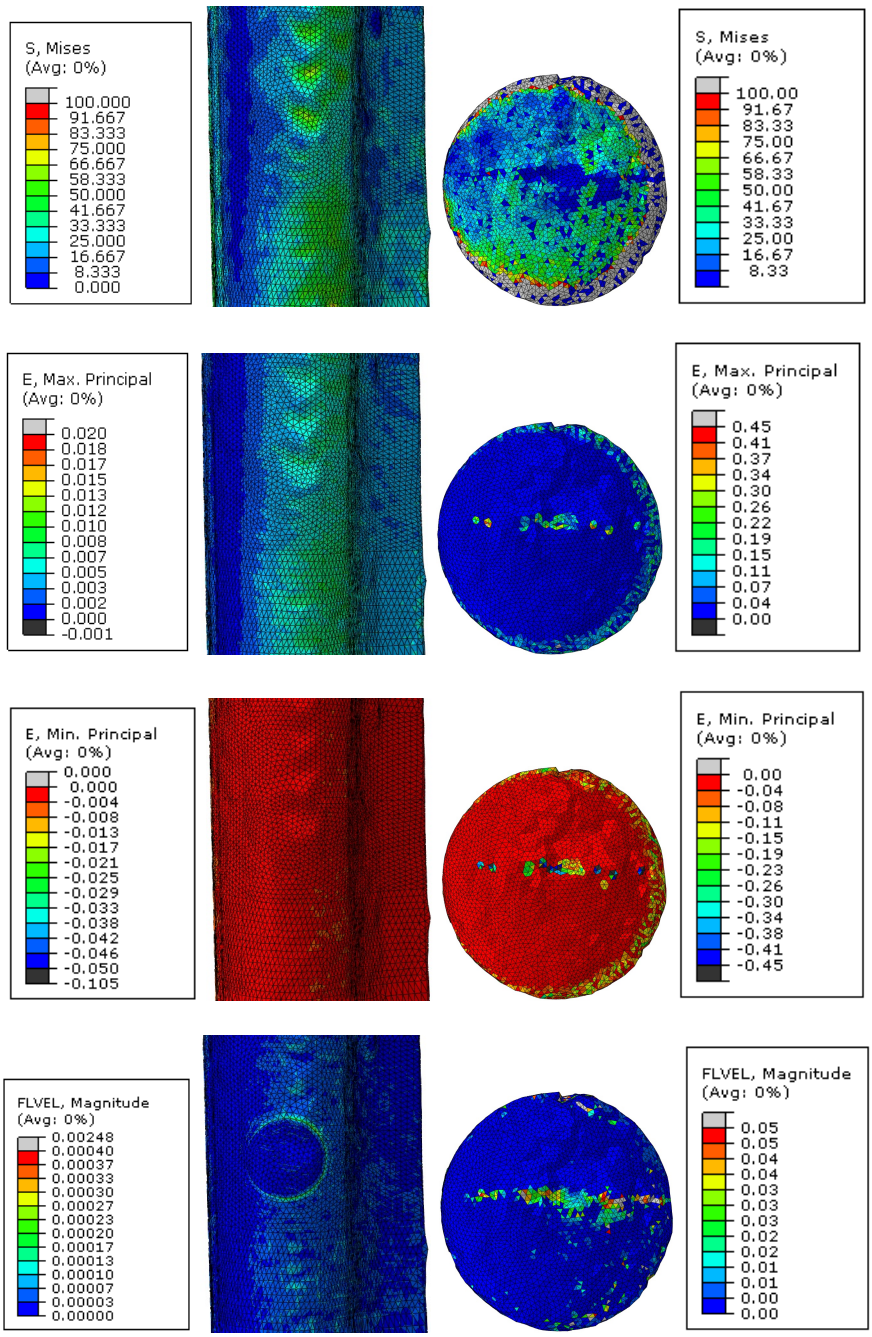

Figure 14: From top to bottom: The von Mises stresses, major principal strain and minor principal strain and fluid velocity during climbing up stairs. To the left the organ model and to the right the micro model.

.

The largest von Mises stress and principal strains were registered on the external surface of the micro model. The elements assigned as soft tissue and representing the crack are experiencing lower von Mises stresses, an increased major principal strains and an increased fluid velocity compared to the rest of the elements representing the bone (except for the elements at the outer shell of the micro model), which can be seen in figures to the right in figure 13 and 14.

Although no elements actually are subjected to pure loads in tension or compression, a larger absolute value of the major principal strain than minor principal strain implies tensile loads. Studying the organ model within figure 13 and 14, it can be seen that the absolute value of the major principal strain is higher than the minor principal strain. By other words the presented elements of the organ model are mainly under the influence of tensile loads. Similar pattern was seen for the bony material of the micro model.

Studying the frontal surface of the circular area of the pre-surgery organ model (left hand side of figure 13 and 14) and compare it with the frontal view of the micro model (right hand side of figure 13 and 14), it was seen that the von Mises stress, the principal strains and fluid velocity distribution within the bony material varies between the roughly the same limits, see table 11. Which concludes a strong connection of the multiscale model.

Parameter	Organ model	Micro model
von Mises (MPa)	0.0 - 58.3	0.0 - 66.7
Major principal. strain (%)	0.0 - 0.7	0.0 - 0.8
Minor principal strain (%)	(-0.3) - 0.0	(-0.4) - 0.0
Fluid velocity (μm/s)	0.000 - 0.042	0.000 - 0.075

Table 11: Comparing the values of the frontal view of the organ- and micro model.

The von Mises stress and principal strains of the organ model in figure 13 and 14 predicted almost equal numbers in the case of fast walking and stair climbing respectively. In order to confirm this, each element within the region of stress fracture, pre-surgery organ model, was studied sepa-

rately for the two presented activities. Within each element the von Mises stress and the major-\minor principal strain was compared between fast walking and climbing stairs. An average value between the two activities was calculated to 3.74MPa (von Mises stress), 0.0355% (major principal strain) and -0.0137% (minor principal strain). Similar numbers were seen between the walking activities and the climbing activities. The result for the other two activities (normal walking and climbing down stairs) is presented in appendix.

The maximum values of the von Mises stress and principal strain are registered at the location where the load is applied to the femoral head, same result is registered both pre- and post-surgery.

5.1.1 Micro model

The predicted displacement from the organ model (table 10) was transferred and applied to the boundary surface of the micro model. In figure 15 the von Mises (MPa), major- and minor principal strains and the fluid velocity (mm/s) concentration of the elements assigned as soft tissue and the crack are presented. The presented results are based on the activity, fast walking and climbing up stairs. The image to the left show the distribution based on the loading case of fast walking and the image to the right is based on climbing up stairs.

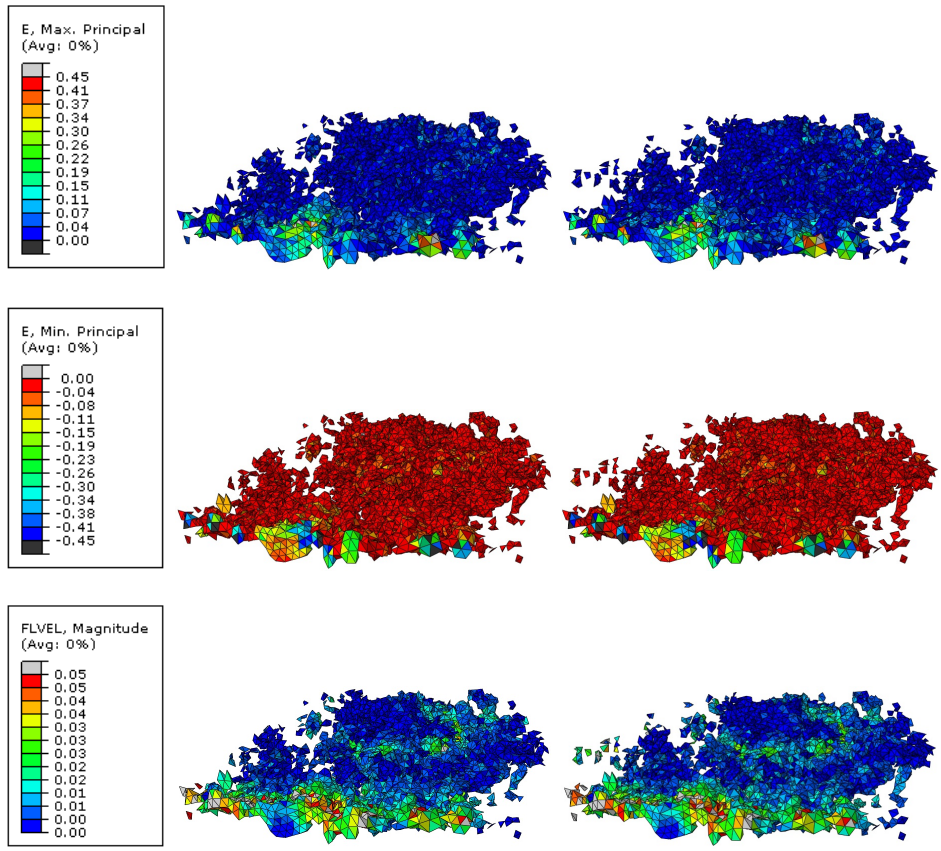

Figure 15: From top to bottom: Principal strains and fluid velocity distribution during climbing up stairs.

The elements representing the soft tissue of the crack showed a larger variation in principal strains and fluid velocities. The variation for each activity and the average value have been summarized and are being shown in table 12. The largest predicted variation between the lowest and the highest values of the major principal strain, octahedral strain and fluid velocity was generated during climbing up stairs followed by climbing down stairs. In other words, climbing stairs is more strenuous on the stress fracture than walking with different paces. The lowest average values was seen during normal walking.

The major- and minor principal strain within the figures show that the

Activity	Major Principal Strain (%)		Minor Principal Strain (%)	
	average	min. & max.	average	min. & max.
Normal Walking	1.9	(-1.1) - 115.7	-1.7	(-99.4) - 1.3
Fast walking	1.9	(-1.1) - 117.0	-1.7	(-101.1) - 1.3
Down Stairs	2.0	(-1.2) - 120.0	-1.8	(-103.0) - 1.4
Up stairs	2.1	(-1.3) - 126.3	-1.8	(-107.7) - 1.6

	Octahedral strain (%)		Fluid velocity (μm/s)	
	average	max.	average	max.
Normal Walking	3.1	175.6	5.5	122.6
Fast walking	3.0	177.7	5.4	124.6
Down Stairs	3.1	182.1	5.6	126.3
Up stairs	3.5	191.0	5.8	156.5

Table 12: Major-, minor principal strain, octahedral strain- and fluid velocity variation in the crack for different activity. The maximum values for the major principal strain and fluid velocity, in the table were registered for the elements with a red colour. Whereas the minimum values of the minor principal strain has a blue colour in figure 12.

elements representing the crack are under the influence of almost equal principal strains. Hence, the crack is under the influence of both tensile and compressive strains. However, when the values of table 12 was studied, a larger predicted absolute major principal strain than minor for both the average value and a span of variation was seen. Hence, the crack is mainly under the influenced tensile load than compressive. Although no elements actually are subjected to pure loads in tension or compression.

5.2 Post-surgery

The circular areas in the centre of figures 16 and 17 represent the location of the biopsy, the presented figures show the von Mises stress (MPa), principal strains and fluid velocity (mm/s). As the crack is surgically removed these elements change their material parameters from bone- to soft tissue accordingly to table 5.

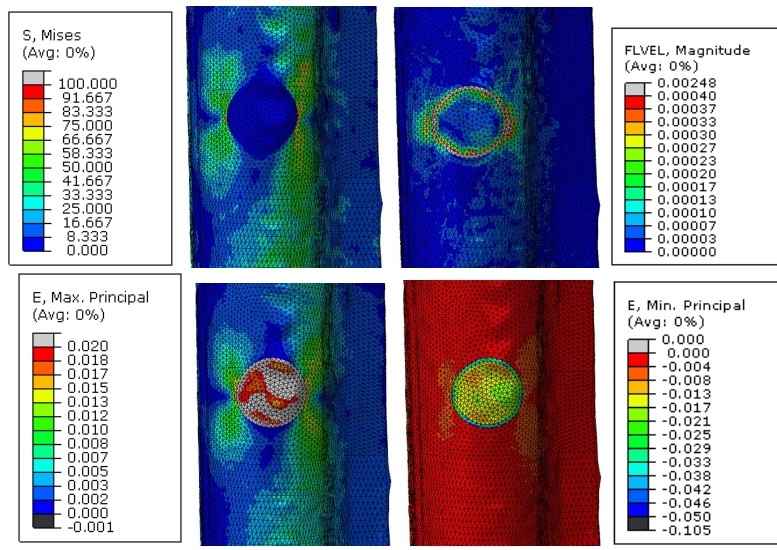

Figure 16: From top to bottom: The von Mises stresses and fluid velocity, major principal strain and minor principal strain during fast walking.

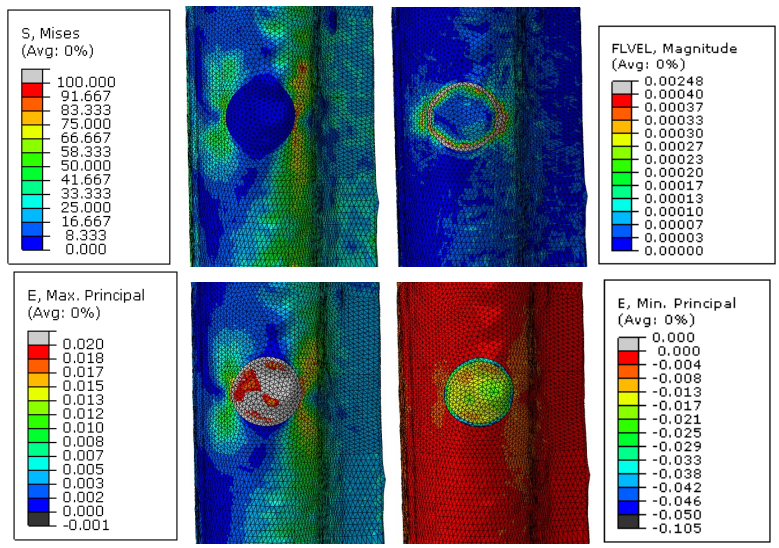

Figure 17: From top to bottom: The von Mises stresses and fluid velocity, major principal strain and minor principal strain during fast walking and climbing up stairs.

Table 13 show the average- and the maximum-\minimum values of the principal strains, octahedral strain and fluid velocity within the elements assigned as soft tissue and representing the area of the removed crack for each activity.
Comparing the result within the soft tissue of the crack (figure 15 and table 12) and the soft tissue of the post-surgery organ model (figure 16 and 17 and table 13) it can be seen that the average value of the major principal strain (16.4%), octahedral shear strain (21.1%) and the fluid velocity (98.6%) decreased after the biopsy was taken.

However, since the inserted intramedullary nail was not modelled within the post-surgery organ model, the stress and strain state in the bone post-surgery is even lower than what is presented in figure 16 and 17.

5.3 Tissue differentiation

The result of the tissue differentiation will be divided by its theory, but also on the scale of resolution. Two different models where studied in which

Activity	Major Principal Strain (%)		Minor Principal Strain (%)	
	average	min. & max.	average	min. & max.
Normal Walking	1.6	0.2 - 4.6	-1.2	(-4.1) - (-0.3)
Fast walking	1.6	0.2 - 4.6	-1.3	(-4.1) - (-0.3)
Down Stairs	1.7	0.2 - 4.8	-1.3	(-4.1) - (-0.3)
Up stairs	1.7	0.2 - 4.8	-1.3	(-4.4) - (-0.4)

	Octahedral strain (%)		Fluid velocity (μm/s)	
	average	min. & max.	average	max.
Normal Walking	2.4	0.6 - 6.6	0.075	0.164
Fast walking	2.5	0.5 - 6.7	0.076	0.166
Down Stairs	2.5	0.5 - 6.9	0.077	0.169
Up stairs	2.6	0.5 - 7.1	0.079	0.174

Table 13: Major-, minor principal strain, octahedral strain- and fluid velocity variation, post-surgery, for different activity.

tissue differentiation theory were applied: the micro model and representing the crack on a micro level pre-surgery and the organ model representing the femur post-surgery. Have in mind that no internal or external support of the organ model was modelled, although it was used during the treatment of the stress fracture.

The generated loads within the elements representing the granulation tissue for both the micro and macro model will determine which tissue will be formed. The formed tissue are only based on the final element-value and not the values over time, i.e. no iterative process was used.

The differentiated tissue will be presented as a percentage of the total amount of elements used within the removed stress fracture (i.e. the organ model), and the crack (i.e. the micro model). The percentage distribution for each tissue can be seen in figures 18 and 19. The diagrams are based on the loading case of climbing up stairs.

5.3.1 Perren and Cordey

A percentage distribution of tissue differentiation according to the theory of Perren and Cordey is presented in figure 18. Figure 18a shows the differentiated tissues for the micro model and 18b the differentiated tissues

for the organ model.

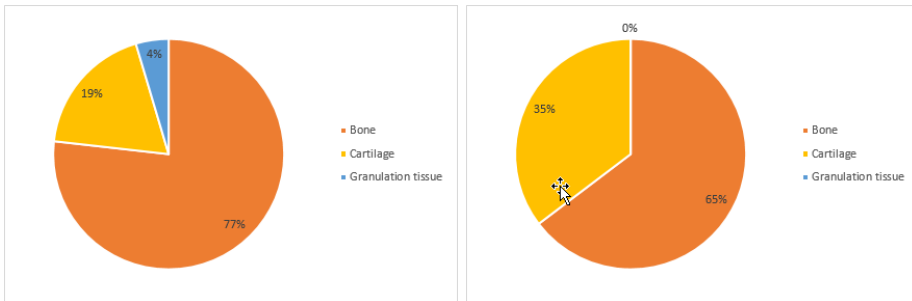

(a) (b)

Figure 18: The differentiated tissue based on theory of Perren and Cordey, in (a) micro model (pre surgery) and (b) organ model (post surgery).

Figure 18a shows that most (77%) of the elements within the crack will differentiate from granulation tissue to bone tissue. 19% differentiated into cartilage, 2% differentiated into fibrous tissue and 2% was unable to differentiate into any other tissue and remained as granulation tissue. Although a large amount of the elements will differentiate into bone, it can be seen in figure 15 that there is a large portion of elements close to the frontal part of the micro model that has a major principal strain above the threshold equal to bone. Hence, these elements will differentiate to either cartilage, fibrous- or granulation tissue.

Similarly figure 18b show that the majority of the elements for the organ model have differentiated to bone (65%), the remaining 35% differentiated to cartilage and will later undergo endochondral ossification.

5.3.2 Prendergast and Huiskes

The tissue differentiation theory of Prendergast and Huiskes predicts that 38% of the elements within the crack will differentiate from granulation tissue into mature bone. Together the formed bone (mature- and immature bone) stand for a total of 55% of the elements and 45% remains as soft tissue (15% cartilage and 30% fibrous tissue) (figure 19a).

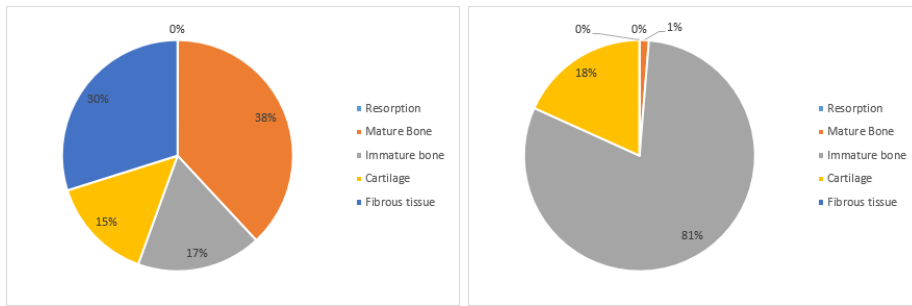

(a) (b)

Figure 19: The differentiated tissue based on theory of Prendergast and Huiskes, in (a) micro model (pre surgery) and (b) organ model (post surgery).

81% of the elements within the organ model had an index within the threshold of immature bone, 1% equals mature bone and 18% differentiated to cartilage. Different to the micro model (figure 19a), the calculated index did not match the threshold of either resorption or fibrous tissue, which can be seen in figure 19b.

6 Discussion

6.1 Summary

The aim of this study was to understand the behaviour of a stress fracture on micro level when it is subjected to loads during daily activity and evaluate the need to model the true crack geometry, in comparison with Fågelberg that modelled an idealized crack. In order to do so a multiscale model on different tiers of resolution were established. Three different models where established during the project: one model representing the femur before surgery and its corresponding micro model and one model representing the femur where a biopsy, removing the stress fracture, have been performed. The organ models were generated using well known and well used techniques (Schileo et al., 2007), whereas the micro model used a grey-scale pixel based technique in order to generate a three dimensional model from μCT-scans. Using the Finite element method, the von Mises stresses, principal strains and fluid velocities were calculated.

6.2 Multiscale model

A finite element multiscale model was established. The von Mises stress, principal strain and fluid velocity in the two models were roughly within the same limits.

The presented principal strain for the organ model in figure 13 and 14, showed that the elements on the lateral side of the femur and close to the area representing the biopsy are mainly loaded in tension. Cristofolini et al. performed a *in vitro* study, evaluating the strain distribution on the proximal human femoral metaphysis. Their study found that the strains measured *in vivo* were compatible with the strains measured *in vitro* (Cristofolini et al., 2009). Cristofolini et al. subjected the femur to different loading conditions representing different activities, the strains were measured with strain gauges and then compared with strains measured *in vivo*. One strain gauge was placed on the lateral side of the proximal diaphysis just below the lesser trochanter. The gauge registered larger strains in tension than compression. Although a different region was studied and the distance between the position of the strain gauge and the location of the stress fracture in the current model are far from each other, it is likely that the strains further down the lateral side would be subjected mainly in tension.

Numerous studies have been done in order to validate strain based finite element bone models with experimental measurements. Predicting strain levels has been shown to be difficult. Reports has shown both promising result (Anderson et al., 2005; Barker et al., 2005; Taddei et al., 2006) and less promising result (Keyak et al., 1993). The works that showed promising result and hade data that fitted well with a statistical model, ($R^2 > 0.8$) usually used a highly manual modelling procedure and relied heavily on the assumptions made on the material properties of bone. Whereas less accurate results ($R^2 < 0.7$) were obtained when a more automated and general material properties of bone was implemented.

The accuracy of the result is believed to be connected to the chosen material model and the modelling procedure (Schileo et al., 2008). The material models and modelling procedure was chosen in such a way that both automated and manual procedures were include and had material relations that had a strong correlation between produced FE models and experimental values (Morgan et al., 2003; Taddei et al., 2007; Schileo et al.,

2007, 2008). The assumptions made resulted in material parameters that matched well with the stiffness of trabecular and cortical bone in literature (Stephen C. Cowin, 2007; Van C. Mow, 1997; Nordin and Frankel, 2012). Therefore the strain and stress state of both the micro and organ models are assumed to be fairly accurate.

Validating the stress, strain and fluid velocity distribution of the micro model proved to be problematic. Mainly because the bone sample has its own unique geometry, which made it almost impossible to compare it to other similar studies. However studying the result within figure 13 and 14 and table 11, it can be seen they vary within roughly the same limit.

Although a connection between the macro model and the micro model was established, it is not flawless. As there are many assumptions done due to position, geometry, material parameters and boundary conditions the result may differ. One of the biggest issues was to get an even displacement distribution over the elements on the boundary surface, which is based on the micro models complex geometry. Due to the geometry a larger portion of elements than intended, were included and subjected with a displacement. Figure 13 and 14, shows that a larger section of elements on the right side of the micro model are experiencing higher principal strains and von Mises stresses than the left side. The consequences on the stress and strain state of the crack have not been evaluated.

Within the elements of interest, both for the organ- and micro model; the von Mises stress, principal strain, octahedral shear strain and fluid velocity distribution was similar between the activities. This is not surprising since all activities evaluated were daily normal activities. Thus, none of the activities was more strenuous on the stress fracture. However climbing stairs had the largest values of principal strains, octahedral shear strains and fluid velocities.

Comparing the stress and strain state of the pre-surgery model with earlier work on FE studies of stress fractures, i.e the master thesis project by (Få gelberg, 2012), may not give any conclusive result. Fågelberg et al. studied a young healthy tibia where no internal fixation was performed post-surgery, whereas the current study focused on the femur of an old lady. However, Fågelberg (2012) concluded that the stresses and strains in the granulation tissues decreased significantly as the stress fracture was removed. Similar results were seen in this project, but to a much lesser extent. The major principal strain decreased with an average of 16% for all

activities, the minor principal strain increased with an average of 27%, the octahedral strain decreased with an average of 21% and the fluid velocity decreased with an average of 99%. Though the stress and strain state of the organ post-surgery model may not be realistic since the nail treatment was not implemented, this is still indicative of the potential effect of the stress-fracture drilling surgery.

6.3 Tissue differentiation

No significant difference within the differentiation result was seen between the activities. However, there are significant differences within the result between the different theories and the pre- and post-surgery models.

The tissue differentiation theory of Pereen and Cordey predicted a different result compared to the theory of Prendergast and Huiskes. The difference is primarily based on the different threshold of the theories and on the fact that the algorithm by Prendergast also accounts for the fluid velocity.

Based on the theory of Prendergast the micro model showed that the majority of the elements predict differentiation to mature bone, whereas the post-surgery model predicts immature bone. The difference between the models are believed to be based on either the fluid velocity or boundary conditions. It was seen at the post-surgery model that the fluid velocity had very low impact on the differentiated tissue compared with the octahedral shear strain. Whereas the octahedral strain within the micro model regulated the differentiation to bone and the fluid velocity regulated the differentiation to soft tissue. Additionally, due to the porosity of the bone surrounding the crack, it was difficult to only identify the elements within the crack. Therefore it is believed that the difference within the result, are based on that elements not representing crack have been included in the study of tissue differentiation. Finally, no parameter describing the pressure boundary condition outside the models was found, this may be a factor that controls the varying fluid velocity of the models.

Pre surgery showed a larger variation in result between the different tissue differentiation theories. All theories predict that the majority of the granulation tissue elements within the crack differentiate into bone, which is contradictory to the work of Fågelberg et al. On the other hand there is a large portion of elements that are under the influence of high principal

strains in tension, octahedral shear strains and fluid velocities, as seen in figure 15. Hence, these elements would differentiate into soft tissue instead of bone as high values of these parameters are believed to promote soft tissue formation (Isaksson et al., 2006).

Post-surgery, the majority of the soft tissue elements is predicted to either differentiate into bone or cartilage. Thus, it suggests that the bone would heal when the stress fracture is removed. In reality, an intramedullary nail was inserted, which further lowered stresses and strains in this patient.

The large variation within the results from the tissue differentiation result are believed to be affected by many parameters and assumptions during the modelling process, such as separating what is the actual crack or not (no distinctive clear crack), no time parameter have been included within the study, geometrical differences within the μCT-images and material- and geometrical modelling. Therefore it is difficult to conclude if the crack heal or not with conservative treatment, based on the presented results.

6.4 Limitations

In real life the femur is not only subjected to loads through joint contact forces, as modelled in the current project. In fact, over 20 different muscles interconnect with the joint contact force (Pedersen et al., 1997). Duda et al. (1998) concluded in an extensive FE study on how muscle forces affected the strain distribution of the femur. Therefore by neglecting major muscles around the femur, the strains in tension and compression are in most cases overestimated. Their study focused on both the contact forces of the hip and knee but also adding the major muscles around the femur. Different load cases were studied, each load case included different sets of muscles. They found that a more simplified load case (including the contact forces, the abductors and the illo-tibial band), predicted principal strain values of close to 0.3%, which matches well with the average principal strain value of the pre surgery organ model (figure 13 and 14). When all the muscles were include, the principal never exceeded 0.2% (Duda et al., 1998). However, as the magnitude of the muscle forces of the specific patient was not recorded, the muscle force parameter was not considered in this study.

Generating an accurate geometry of bone is not trivial, due to its complex geometrical shape. Provided to the project was a set of CT-images both of the hip and femur but also of the removed stress fracture. At some

areas it was difficult to distinguish bone from bone or bone from soft tissue, both as cortex was either too thin or not even visible or there were no clear boarder between the tissues. Therefore, areas representing soft tissue or bone with other properties may been included in the organ-\micro model. This can affect the material properties and the material mapping of bone, which may affect the stress and strain state.

The mesh of both models can always be improved, as a finer mesh provides a more accurate result. Especially within the micro model, where a very complex geometry was studied. Due to the complex geometry, the generated mesh of the micro model was much unstructured and included a large number of elements with bad quality index (distorted or ill shaped). However, as the amount of elements used within the model was already high and the computational time to solve a simulation was roughly fourteen hours, the amount of elements had to be restricted. Within the organ model it would have been wise to model the actual crack, in order to get more realistic displacements.

The multiscale used two different element types: one second order tetrahedral pore pressure element (organ model) and one tetrahedral pore pressure element of the first order (micro model). It is known that the first order tetrahedral elements have slow rate of convergence (Abaqus, 2012). The first order tetrahedral element of the micro model was chosen as this element have been used in an earlier master thesis project that studied the stress-\strain concentration on micro level (Lugo, 2013). When the stress and strain concentration of the organ model was compared with the micro model, it was seen that the von Mises stress, principal strain and fluid velocity were roughly the same within the bony material. Therefore, the effect of using different element types between the models are believed to be minimum.

6.5 Conclusions

A finite element multiscale model between two tiers of resolution was established representing an atypical fracture. Correlation within the von Mises stress and principal strain of the pre-surgery organ- and micro model was seen, although some refinements to the multiscale model might improve the result.

The study concluded that certain areas of the crack pre-surgery, are under the influence of large principal- and octahedral strains and fluid velocities. The parameters within the crack are of such magnitude that the soft tissue undergo large deformation, which therefore describes the poor ability of the stress fractures to heal. Same pattern was seen for each studied activity. It suggest that there is no specific type of activity that is more strenuous in the crack.

As the stress fracture is surgically removed, the majority of the granulation tissue within the removed area differentiate into bone. However, the tissue differentiation of the pre- and post-surgery model does not correspond to the real patient treatment since some modelling aspects was left out.

6.6 Further work

The presented work in this master thesis project is the first finite element multiscale modelling of stress fractures. Therefore this is only a beginning and many improvements can be applied in order to enhance the understanding and the behaviour of stress fractures.

In terms of modelling aspects, a stronger and more even connection between the organ model and the micro model may give a more accurate strain distribution of the crack. Also applying more realistic boundary conditions, a more organized and well-shaped mesh of the micro model are just a few suggestions that could improve the work.

As a very simplified tissue differentiation was studied an iterative healing process of the soft tissue may give a deeper knowledge of stress fractures behaviour and poor ability heal.

7 Appendix

7.1 Organ model

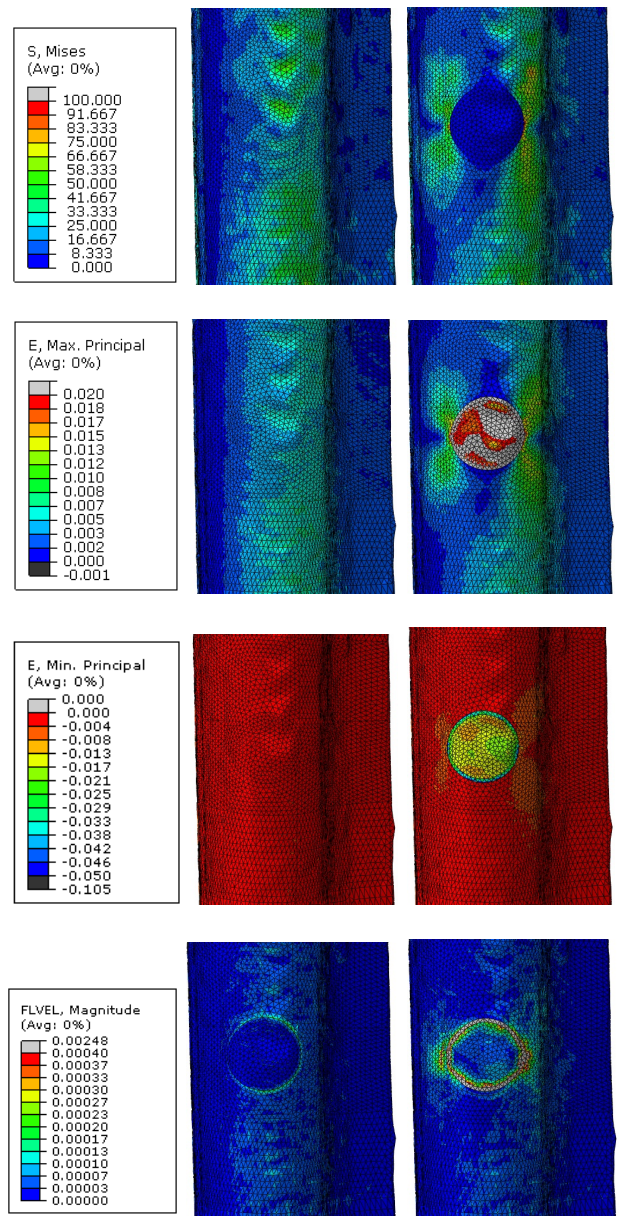

Figure 20: From top to bottom: The von Mises stresses, major principal strain and minor principal strain and fluid velocity during normal walking

.

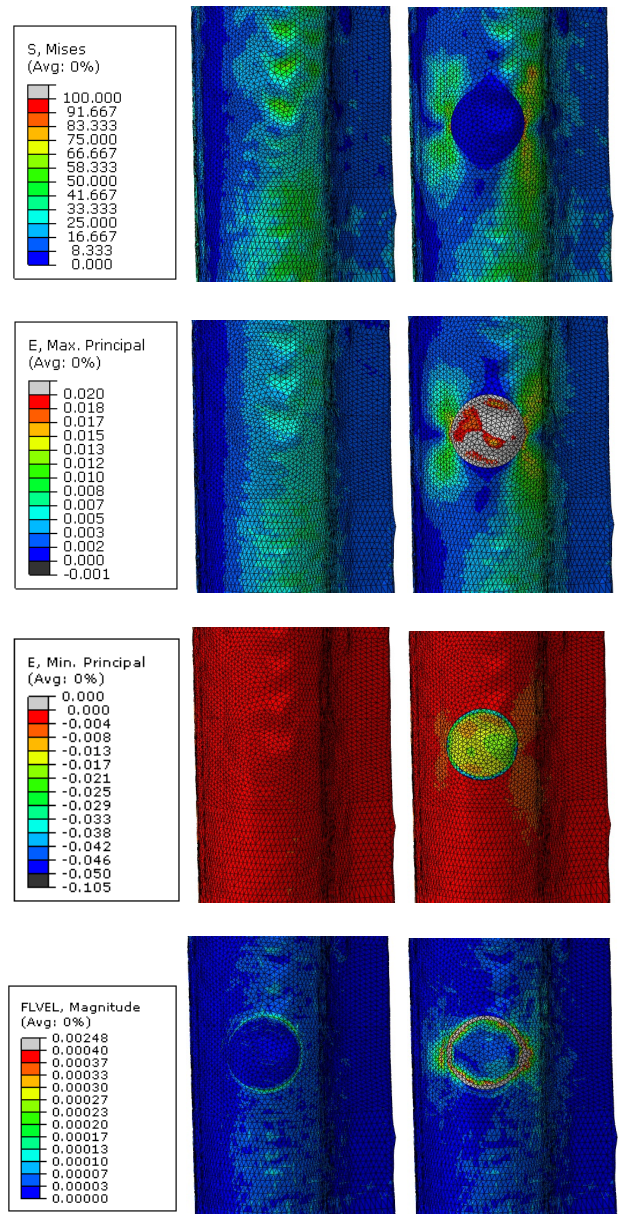

Figure 21: From top to bottom: The von Mises stresses, major principal strain and minor principal strain and fluid velocity during climbing down stairs

7.2 Micro model

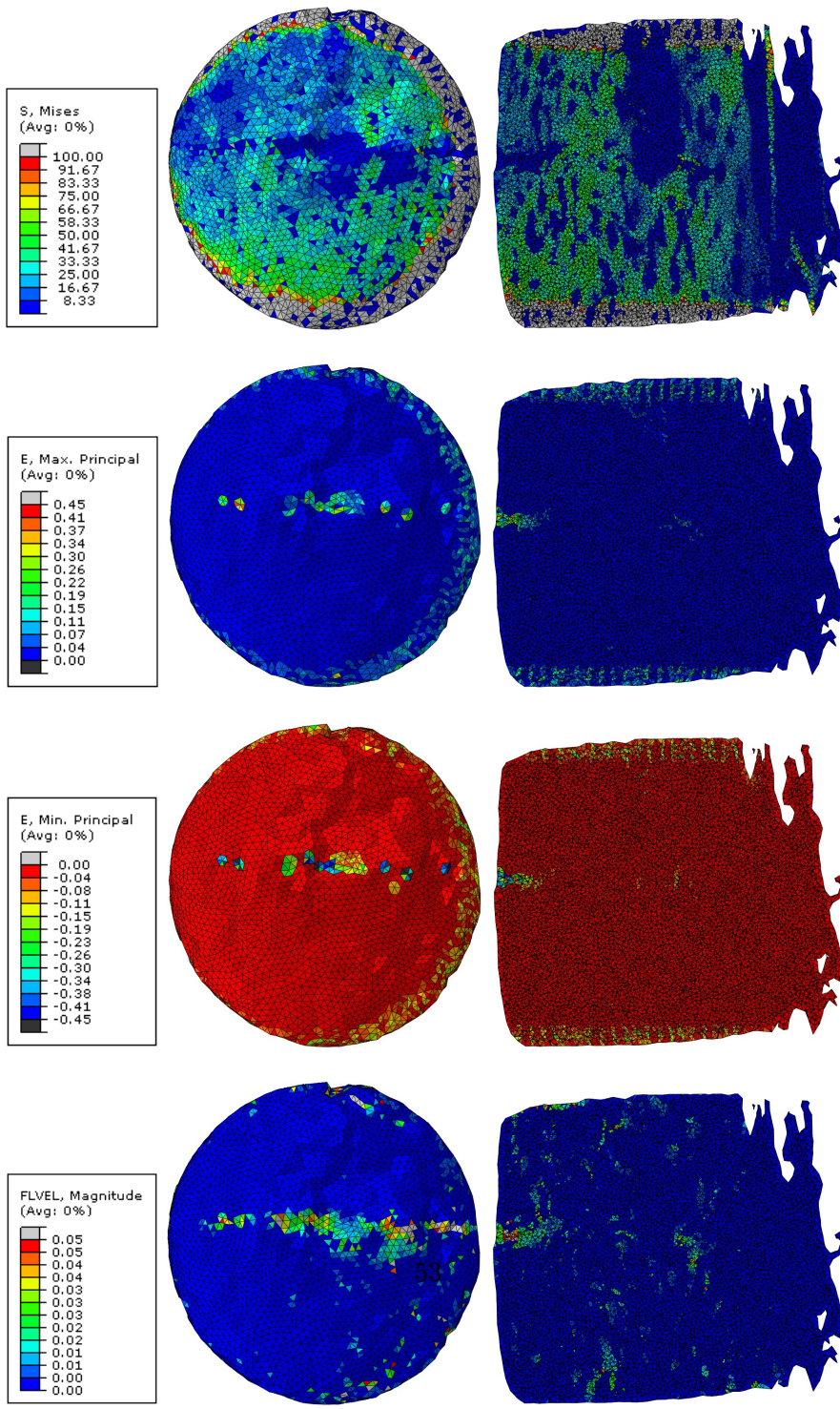

Figure 22: From top to bottom: The von Mises stresses, major principal strain and minor principal strain and fluid velocity during normal walking

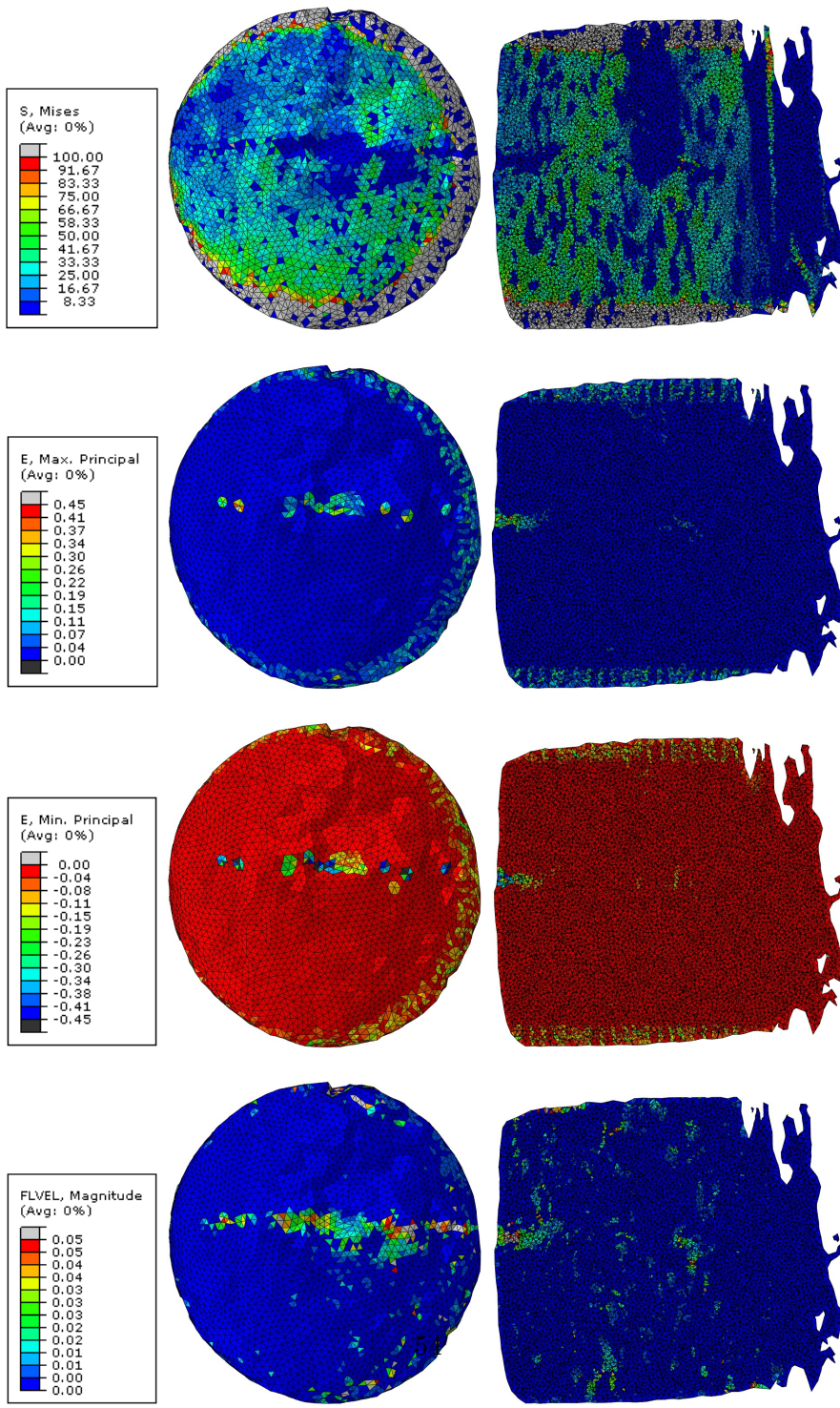

Figure 23: From top to bottom: The von Mises stresses, major principal strain and minor principal strain and fluid velocity during climbing down stairs

References

Abaqus. 2012. *Abaqus Analysis User's Manual*. Dassault Systems.

Anderson, Andrew E., Peters, Christopher L., Tuttle, Benjamin D., and Weiss, Jeffrey a. 2005. Subject-Specific Finite Element Model of the Pelvis: Development, Validation and Sensitivity Studies. *Journal of Biomechanical Engineering*, 127(3):364.

Aspenberg, Per and Schilcher, Jörg. 2014. Atypical femoral fractures, bisphosphonates, and mechanical stress. *Current osteoporosis reports*, 12(2):189–93.

Barker, D S, Netherway, D J, Krishnan, J, and Hearn, T C. 2005. Validation of a finite element model of the human metacarpal. *Medical engineering & physics*, 27(2):103–13.

Bennell, Kim, Matheson, Gordon, Meeuwisse, Willem, and Brukner, Peter. 1999. Risk factors for stress fractures. *Sports medicine*, 28(2):91–122.

Bergmann, G, Deuretzbacher, G, Heller, M, Graichen, F, Rohlmann, A, Strauss, J, and Duda, G N. 2001. Hip contact forces and gait patterns from routine activities. *Journal of biomechanics*, 34(7):859–71.

Biot, Maurice a. 1941. General Theory of Three-Dimensional Consolidation. *Journal of Applied Physics*, 12(2):155.

Blank, S. 1987. Transverse tibial stress fractures. A special problem. *The American journal of sports medicine*, 15(6):597–602.

Bosemark, Per, Isaksson, Hanna, McDonald, Michelle M, Little, David G, and Tägil, Magnus. 2013. Augmentation of autologous bone graft by a combination of bone morphogenic protein and bisphosphonate increased both callus volume and strength. *Acta orthopaedica*, 84(1):106–11.

Claes, L E and Heigele, C a. 1999. Magnitudes of local stress and strain along bony surfaces predict the course and type of fracture healing. *Journal of biomechanics*, 32(3):255–66.

Cristofolini, L, Juszczyk, M, Taddei, F, and Viceconti, M. 2009. Strain distribution in the proximal human femoral metaphysis. *Proceedings of*

the Institution of Mechanical Engineers. Part H, Journal of engineering in medicine, 223(3):273–88.

Cristofolini, Luca, Conti, Giorgia, Juszczyk, Mateusz, Cremonini, Sara, Van Sint Jan, Serge, and Viceconti, Marco. 2010. Structural behaviour and strain distribution of the long bones of the human lower limbs. *Journal of biomechanics*, 43(5):826–35.

Duda, G N, Heller, M, Albinger, J, Schulz, O, Schneider, E, and Claes, L. 1998. Influence of muscle forces on femoral strain distribution. *Journal of biomechanics*, 31(9):841–6.

Få gelberg, Emil. 2012. Mechanical analysis of tibial stress fractures : A finite element study investigating the potential of a new surgical treatment. Technical report, Lund University.

Fang, Q and Boas, DA. 2009. Tetrahedral mesh generation from volumetric binary and grayscale images. *Biomedical Imaging: From Nano to Macro*, pages 1142–1145.

Huiskes, R., van Driel, W.D., Prendergast, P., and Sø balle, K. 1997. A biomechanical regulatory model for periprosthetic fibrous-tissue differentiation. *Journal of Material Science*, pages 785–788.

Isaksson, Hanna, Wilson, Wouter, van Donkelaar, Corrinus C, Huiskes, Rik, and Ito, Keita. 2006. Comparison of biophysical stimuli for mechano-regulation of tissue differentiation during fracture healing. *Journal of biomechanics*, 39(8):1507–16.

Kalender, W a, Felsenberg, D, Genant, H K, Fischer, M, Dequeker, J, and Reeve, J. 1995. The European Spine Phantom–a tool for standardization and quality control in spinal bone mineral measurements by DXA and QCT. *European journal of radiology*, 20(2):83–92.

Kass, M, Witkin, A, and Terzopoulos, D. 1988. Snakes: Active contour models. *International journal of computer vision*, 331:321–331.

Keyak, J H, Fourkas, M G, Meagher, J M, and Skinner, H B. 1993. Validation of an automated method of three-dimensional finite element modelling of bone. *Journal of biomedical engineering*, 15(6):505–9.

Lugo, Neis. 2013. Estimation of cortical bone strength using finite element analyses: the role of elastic properties, image resolution and bone porosity. Technical report, Lund University.

Mckibbin, B. 1978. The biology of fracture healing in long bones. *THE JOURNAL OF BONE AND JOINT SURGERY*, 60-B.

Morgan, Elise F., Bayraktar, Harun H., and Keaveny, Tony M. 2003. Trabecular bone modulus–density relationships depend on anatomic site. *Journal of Biomechanics*, 36(7):897–904.

Morgan, Elise F, Mason, Zachary D, Chien, Karen B, Pfeiffer, Anthony J, Barnes, George L, Einhorn, Thomas a, and Gerstenfeld, Louis C. 2009. Micro-computed tomography assessment of fracture healing: relationships among callus structure, composition, and mechanical function. *Bone*, 44(2):335–44.

Nordin, Margareta and Frankel, Victor H. 2012. *Basic Biomechanics of the Musculoskeletal System.* Lippincott Williams & Wilkins, Philadelphia, fourth edition.

Pauwels, Friedrich. 1960. *A new theory on the influence of mechanical stimuli on the differentiation of supporting tissue.* Z Anat Entwicklungsgesch, Berlin.

Pedersen, DR, Brand, RA, and Davy, DT. 1997. Pelvic muscle and acetabular contact forces during gait. *Journal of biomechanics*, 9290(97).

Perren, S. M. 1979. Physical and Biological Aspects of Fracture Healing with Special Reference to Internal Fixation. *Clinical Orthopaedics and Related Research*, 138:175–196.

Prendergast, PJ, Huiskes, R, and Sø balle, K. 1997. Biophysical stimuli on cells during tissue differentiation at implant interfaces. *Journal of biomechanics*.

R. Bruce Martin, David B. Burr and Sharkey, Neil A. 1998. *Skeletal Tissue Mechanics.* Springer, New York.

Rho, J Y, Kuhn-Spearing, L, and Zioupos, P. 1998. Mechanical properties and the hierarchical structure of bone. *Medical engineering & physics*, 20(2):92–102.

Schilcher, Jörg and Aspenberg, Per. 2009. Incidence of stress fractures of the femoral shaft in women treated with bisphosphonate. *Acta orthopaedica*, 80(4):413–5.

Schilcher, Jörg, Michaelsson, Karl, and Aspenberg, Per. 2011. Bisphosphonate use and atypical fractures of the femoral shaft. *New England Journal of Medicine*.

Schilcher, Jörg, Sandberg, Olof, Isaksson, Hanna, and Aspenberg, Per. 2014. Histology of 8 atypical femoral fractures. *Acta orthopaedica*, 85 (3):1–7.

Schileo, Enrico, Taddei, Fulvia, Malandrino, Andrea, Cristofolini, Luca, and Viceconti, Marco. 2007. Subject-specific finite element models can accurately predict strain levels in long bones. *Journal of biomechanics*, 40(13):2982–9.

Schileo, Enrico, Dall'ara, Enrico, Taddei, Fulvia, Malandrino, Andrea, Schotkamp, Tom, Baleani, Massimiliano, and Viceconti, Marco. 2008. An accurate estimation of bone density improves the accuracy of subject-specific finite element models. *Journal of biomechanics*, 41(11):2483–91.

Schindelin, Johannes, Arganda-Carreras, Ignacio, Frise, Erwin, Kaynig, Verena, Longair, Mark, Pietzsch, Tobias, Preibisch, Stephan, Rueden, Curtis, Saalfeld, Stephan, Schmid, Benjamin, Tinevez, Jean-Yves, White, Daniel James, Hartenstein, Volker, Eliceiri, Kevin, Tomancak, Pavel, and Cardona, Albert. 2012. Fiji: an open-source platform for biological-image analysis. *Nature methods*, 9(7):676–82.

Snyder, S M and Schneider, E. 1991. Estimation of mechanical properties of cortical bone by computed tomography. *Journal of orthopaedic research : official publication of the Orthopaedic Research Society*, 9(3):422–31.

Stephen C. Cowin, Stephen B. Doty. 2007. *Tissue Mechanics*. Springer, New York.

Taddei, Fulvia, Pancanti, Alberto, and Viceconti, Marco. 2004. An improved method for the automatic mapping of computed tomography numbers onto finite element models. *Medical Engineering & Physics*, 26(1):61–69.

Taddei, Fulvia, Cristofolini, Luca, Martelli, Saulo, Gill, H S, and Viceconti, Marco. 2006. Subject-specific finite element models of long bones: An in vitro evaluation of the overall accuracy. *Journal of biomechanics*, 39 (13):2457–67.

Taddei, Fulvia, Schileo, Enrico, Helgason, Benedikt, Cristofolini, Luca, and Viceconti, Marco. 2007. The material mapping strategy influences the accuracy of CT-based finite element models of bones: an evaluation against experimental measurements. *Medical engineering & physics*, 29 (9):973–9.

Thesleff, Alexander. 2013. Stress fracture at the anterior tibia : A finite element analysis of adaptive healing over time. Technical report, Lund University.

Van C. Mow, Wilson C. Hayes. 1997. *Basic Orthopaedic Biomechanics*. Lippincott Williams & Wilkins, Philadelphia, second edition.

Viceconti, M and Taddei, F. 2003. Automatic generation of finite element meshes from computed tomography data. *Critical Reviews^{TM} in Biomedical Engineering*, 31(1 & 2):27–64.

Waarsing, Jan H, Day, Judd S, and Weinans, Harrie. 2004. An improved segmentation method for in vivo microCT imaging. *Journal of bone and mineral research : the official journal of the American Society for Bone and Mineral Research*, 19(10):1640–50.

Walpole, Joseph, Papin, Jason a, and Peirce, Shayn M. 2013. Multiscale computational models of complex biological systems. *Annual review of biomedical engineering*, 15:137–54.

Warden, Stuart J, Burr, David B, and Brukner, Peter D. 2006. Stress fractures: pathophysiology, epidemiology, and risk factors. *Current osteoporosis reports*, 4(3):103–9.

Yushkevich, Paul A, Piven, Joseph, Hazlett, Heather Cody, Smith, Rachel Gimpel, Ho, Sean, Gee, James C, and Gerig, Guido. 2006. User-guided 3D active contour segmentation of anatomical structures: significantly improved efficiency and reliability. *NeuroImage*, 31(3):1116–28.